Ocean Engineering 250 (2022) 111062

Contents lists available at ScienceDirect

Ocean Engineering

journal homepage: www.elsevier.com/locate/oceaneng

Wakes and free surface signatures of a generic submarine in the homogeneous and linearly stratified fluid

Fenglai Huang [a], Qingjie Meng [b], Liushuai Cao [a,*], Decheng Wan [a,c]

[a] Computational Marine Hydrodynamics Lab (CMHL), State Key Laboratory of Ocean Engineering, School of Naval Architecture, Ocean and Civil Engineering, Shanghai Jiao Tong University, Shanghai, 200240, China
[b] Wuhan Second Ship Design and Research Institute, Wuhan, 430064, China
[c] Ocean College, Zhejiang University, Zhoushan, 316021, China

ARTICLE INFO

Keywords:
Submarine
Stratified Fluid
Wakes
Free Surface Signatures
CFD

ABSTRACT

In this paper, a generic submarine Joubert BB2 model travels both in the homogenous and linearly stratified fluid are simulated and investigated. The stable stratification of background density is achieved by specifying the linearly distributed temperature based on a thermocline model. Four main aspects are chosen to discuss the specialty of stratified fluid characteristics by comparing the drag force, downstream wakes, internal waves, and free surface signatures with those of the homogeneous condition. The results show that due to the density gradient and internal waves generation and propagation in the stratified flow, the resistance of the submarine increases. Because of the vertical confinement induced by buoyancy in the stratified environment, the velocity decays faster, thus leading to a broader spread range of wakes in the horizontal plane than the vertical plane. Furthermore, internal waves and anisotropic turbulence stimulated by the moving submarine result in specific signatures on the water surface. A noteworthy anisotropy of the surface wave crest and trough, and a larger influencing zone of the Kelvin waves are shown for the stratified case.

1. Introduction

Stratified flows, common in environmental and geophysical applications, are characterized by the variation of fluid density in the vertical direction. Density stratification is an essential feature of oceans and the atmosphere. Generally, a stably stratified fluid can support internal waves, instabilities, and turbulence that play a critical role in transport and mixing (Armenio and Sarkar, 2005). For example, in the ocean, stratified turbulence mediates the upward transport of bottom water, nutrients, chemical and biological species, and pollutants, while in the atmosphere, stratification affects the transport of pollutants released at ground level. There are a bunch of examples that show the analysis of stratified flows is of broad interest in geophysical (Pedlosky, 1979), industrial (Taitel et al., 1995), and environmental applications (Barat and Cot, 1992).

Wakes of bluff bodies in homogenous fluid have been a central point of many fluid dynamists and engineers as they provide basic flow phenomena and explanations associated with practical applications. The wake dynamics depend strongly on the Reynolds number, defined as the ratio of the inertia force to the viscous forces.

$$Re = \frac{UD}{\upsilon} \tag{1}$$

here, U is the body speed, D is the diameter of the sphere, and υ is the kinematic viscosity of the water. The characteristics of wakes are susceptible to the Reynolds number. For example, the wakes of a sphere can be divided into four regimes as discussed in Sakamoto and Haniu (1990) and Yun et al. (2006).

However, besides the competing effects of inertial and viscous forces, the buoyancy effect can not be neglectable for wakes in a stratified fluid. The internal Froude number Fr is defined as the ratio of the inertia force to the buoyancy force to characterize the different levels of stratification.

$$Fr = \frac{U}{ND} \tag{2}$$

$$N = [-(g/\rho_0)(\partial\rho/\partial z)]^{1/2}$$

where N is the Brunt-Vaisala frequency, ρ_0 is the undisturbed density profile, and g is the gravitational acceleration. Generally, these two crucial parameters, the Reynolds number Re and the internal Froude

* Corresponding author.
E-mail address: liushuaicao@sjtu.edu.cn (L. Cao).

https://doi.org/10.1016/j.oceaneng.2022.111062
Received 13 October 2021; Received in revised form 5 March 2022; Accepted 6 March 2022
Available online 15 March 2022

Nomenclature

B	— The beam of the Joubert BB2 submarine
c_1	— The temperature gradient
c_2	— The density gradient
C_f	— The skin-friction coefficient
C_p	— The pressure coefficient
D	— Depth from draft to duck of the Joubert BB2 submarine
D_{sail}	— Depth from draft to duck of the Joubert BB2 submarine
$\boldsymbol{f}$	— Large-scale force required to maintain the turbulence
Fr	— Froude number
$\boldsymbol{g}$	— Acceleration of gravity
K, M, N	— Moments in x, y, and z direction
K', M', N'	— Non-dimensional moments in x, y, and z direction
L	— The length of the Joubert BB2 submarine
L_H	— The half-width of the evolution of wakes
L_V	— The half-height of the evolution of wakes
N	— The Brunt-Vaisala frequency
P	— Pressure
P_h	— Pressure at the depth of the submarine below the free surface
q	— The volume fraction
r_G	— The grid refinement ratio
Re	— Reynolds number
S_{wa}	— The wetted surface area of the Joubert BB2 submarine
t	— Time
T	— The fluid temperature
T'	— Temperature fluctuation
T_0	— The initial fluid temperature
TKE	— Turbulent kinetic energy
$\boldsymbol{u}$	— Instantaneous velocity vector $(u, v, w)^T$
U	— Initial free stream velocity
U_d	— The centerline velocity deficit
V	— A particle with volume
x, y, z	— Cartesian coordinates
X, Y, Z	— Forces in x, y, and z direction
X', Y', Z'	— Non-dimensional forces in x, y, and z direction
$y+$	— Y-plus, measurement of the first node height near the BB2 submarine
z	— Height of the submarine below the free surface
α	— Thermal diffusivity
β	— Volumetric expansion coefficient
Δt	— Time step
Δ_z, ω_z	— The gradient quantities of the two horizontal velocity components
υ	— Kinematic viscosity
ρ_h	— The fluid density at the depth of the submarine below the free surface
ρ_0	— The initial fluid density
τ_w	— The wall stress

number Fr in a stratified flow affect wakes together.

At the very beginning, experimental methods are mainly adopted to investigate the wakes of the stratified fluid. As Lin and Pao (1979) reviewed, most of the early experimental works on wakes generated by moving bodies of simple geometries like a grid, a two-dimensional body, and an axisymmetric body in the stratified fluid showed that many specific phenomena such as upstream wake blocking, wake collapse, and horizontal vortices observed in stratified wakes are the direct and indirect consequence of the inhibition of vertical motion. Since then, various experimental techniques have been adopted to characterize the wakes and internal waves (Hopfinger et al., 1991; Sysoeva and Chashechkin, 1991; Lin et al., 1992; Chomaz et al., 1993; Bonneton et al., 1993; Wei et al., 2005; Wei et al., 2009). They found that when the time scale of the wake motion approaches the Brunt-Vaisala period, the wake will be influenced by stratification. In particular, stratified wakes would be dramatically different when compared with a non-stratified fluid when turbulence is present. However, due to experimental difficulties of modeling spatially and temporally growing structure in finite-sized facilities, until Spedding (1997), who designed experiments purposeful aiming to the stable, long-lived late-wake structure and distinguished three wake regimes in the evolution of high-Fr wakes of a sphere: (1) a 3D regime (3D), where the wake is unaffected by buoyancy and behaves as an unstratified wake; (2) a nonequilibrium regime (NEQ), where buoyancy forces start suppressing vertical motions; (3) a quasi-two-dimensional regime (Q2D) where buoyancy forces dominate the flow, and the flow organizes into pancake eddies. Later, Meunier et al. (2006) added two new regimes: a buoyancy-controlled (BC) regime as distinct from the NEQ regime at very high Reynold numbers and a viscous 3D regime observed at very late stages. However, subsequent studies have confirmed the existence of these stages, the transition points between successive regimes are not strictly consistent, and the applicability of these regimes to turbulence statistics is unclear.

With the advent of computing power and numerical algorithms, researchers began to undertake numerical simulations in a stratified fluid. As for stratified fluid past a sphere, Gourlay et al. (2001) first used direct numerical simulation (DNS) to simulate a stratified wake and found that pancake vortices emerge in the late regimes independent of the initial conditions. Dommermuth et al. (2002) developed an improved method base on LES and further characterized the wakes. Later, Brucker and Sarkar (2010) compared a towed sphere and a self-propelled spheroid wakes at $Re = 5 \times 10^4$ using LES. Diamessis et al. (2011) employed implicit LES to characterize wake evolution over a broad range of Froude ($2 < Fr < 32$) and Reynolds ($5 \times 10^3 < Re < 10^6$) numbers. The authors found that in the self-propelled case, the mean velocity decayed more rapidly than for the towed case, resulting in a faster rate of energy transfer to the turbulence field due to the higher shear. Pal et al. (2017) found that in the transition from the 3D regime to the non-equilibrium regime, $N\,t = \pi$ marks a vital transition point where oscillatory modulation of the wake existed. More concerning works about stratified flow past a sphere are in Orr et al. (2015), Pal et al. (2016), Chongsiripinyo et al. (2017).

The above works are all limited to stratified flow past a sphere. Behinds the sphere, Ortiz-Tarin et al. (2019) simulated a prolate spheroid with an aspect ratio of the body $L/D = 4$ to investigate the effect of ambient stratification by using Large-eddy simulation (LES). He concluded that the flow past a slender body exhibits more substantial buoyancy effects relative to a bluff body. Niu et al. (2017) simulated the stratified flow past a cylinder at different stratification level and compared with experiment. Mercier et al. (2020) presented the settling dynamics of a disk of finite thickness evolving in a linearly stratified fluid.

Although significant progress has been made in the stratified fluid, most previous studies mainly focused on standard simple geometries, such as the sphere, cylinder, disk, and a prolate spheroid. Fundamental investigations on the flow field around marine vessels are usually studied by ignoring the effect of stratification for simplicity. Numerous computational studies on the wakes of under vessels are available in the literature after the Reynolds-averaged Navier-Stokes (RANS) equations are solved considering the computational cost. (Cao et al., 2016; Gao et al., 2018; Zhang et al., 2019). The detached eddy simulation (DES) is gradually adopted with the advent of computing power (Zhihua et al., 2011; Chase and Carrica, 2013). Due to the high computational cost, the LES method for computing wakes at relatively high Reynolds numbers was introduced only recently. For example, Kumar and Mahesh (2018)

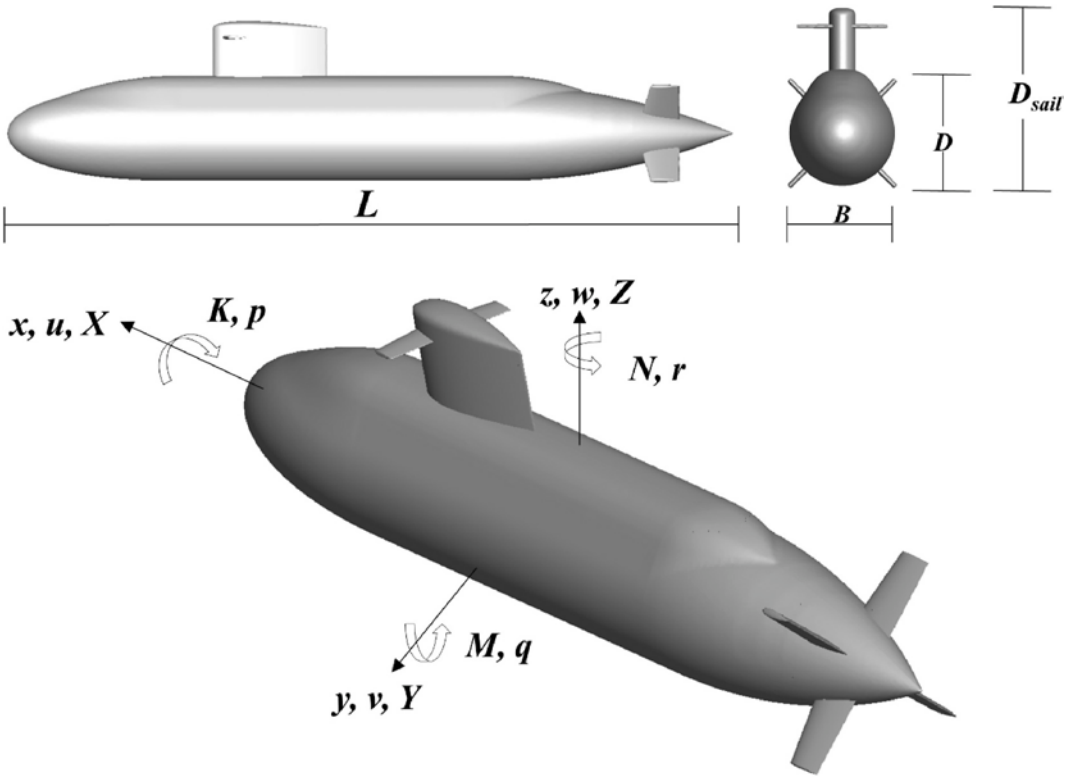

Fig. 1. The Joubert BB2 geometry.

Table 1
Main parameters of BB2 (model scale 1:18.348).

Description	Symbol	Scale	
		Full	Model
Length	L (m)	70.2	3.8260
Beam	B (m)	9.6	0.5232
Draft to Duck	D (m)	10.6	0.5777
Draft to Sail top	D_{sail} (m)	16.2	0.8829
Wetted surface area	S_{wa} (m^2)	2142.3	6.3635

carried out wall-resolved LES on the bare hull at $Re = 1.1 \times 10^6$. Posa and Balaras (2020) have studied the near wakes of the DARPA suboff body at two Reynolds numbers: $Re = 12 \times 10^6$ and $Re = 1.2 \times 10^6$.

Until recently, several works have been trying to simulate the ship (Esmaeilpour, 2017; Li et al., 2019) and submerged bodies (Carrica et al., 2019; Xue et al., 2020; Liu et al., 2020; Ma et al., 2018, 2020) moving in a stratified fluid. These works including Carrica et al. (2019) presented CFD simulations of self-propulsion near the surface in calm water and waves; Xue et al. (2020) investigated the relationship between the motion state of moving submerged bodies and wakes; Liu et al. (2020) discussed the influence of forwarding speed, different positions, and density of the lower layer on resistance and wake of an underwater submarine in density-stratified fluid; Ma et al. (2018) and Ma et al. (2020) tried to quantitatively analyze the effects of submarine speed, depth, and density gradient on the free surface wave pattern in the linearly stratified fluid. However, wakes behinds the underwater vehicles have received more attention rather than the free surface signatures. When submarines travel in the stably stratified environment, the internal waves and anisotropic turbulence produced by the moving submarine will cause roughness variations on the free surface. These characteristics will be detected by the synthetic aperture radar. This motivates the present study of linearly stratified flow past a generic submarine model with a free surface. This work aims to examine the effect of stratification by comparing results with the unstratified case in a relatively high Reynolds number. Unlike previous studies, which focus on simple geometries, the current analysis will concentrate on how the buoyancy effect influences the downstream wakes, density fluctuations between isopycnals, internal waves, and the free surface waves when referring to a complex submarine.

The paper is organized as follows. Test geometry is provided in section 2. In sections 3 and 4, we introduced and validated the numerical method based on a thermocline model to achieve density and temperature stratification. Section 5 discussed the specialty in the stratified fluid by comparing the drag force, downstream wakes, density fluctuations, internal waves and free surface waves with the unstratified case. This part aims to elucidate the stratified flow's buoyancy effects, particularly when a complex geometry moves in the weakly stratified environment with a high Reynolds number. Finally, the conclusions are drawn.

2. The Joubert BB2 submarine model

The platform under study is the Joubert BB2 submarine model. It is a modified version of the Joubert BB1 designed by Joubert (2006), which is now an international benchmark for underwater vehicles. The hydrodynamic studies on BB2 have been tested by several research groups, including free sailing maneuvering model tests performed at the Maritime Research Institute Netherlands (MARIN) and various kinds of CFD solvers (citation(s) 'Torunski, 2018' has/have been changed to match the date in the reference list. Please check here and in subsequent occurrences, and correct if necessary.>Torunski, 2016; Donadei, 2019 and Bettle, 2020).

For consistency with international collaborative work, there are two coordinate systems adopted in this paper. For computational use, the origin of the Cartesian coordinate system is located at the front of the submarine. The x-axis is the normal flow direction, the y-axis points in the starboard direction, and the z-axis points towards the air. Another coordinate system is used for evaluating hydrodynamic forces X, Y, Z and moments K, M, N. It has the same orientation as the computational

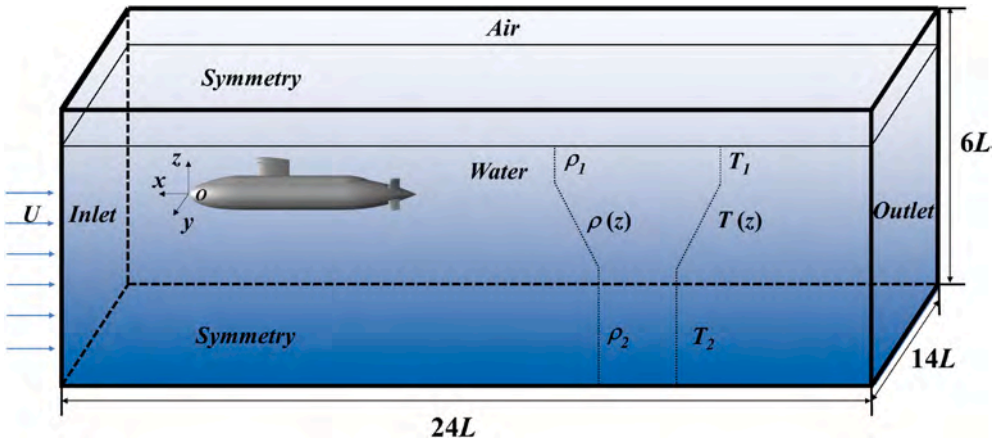

Fig. 2. Domain features and dimensions.

coordinate system, but the origin is located at midship. Fig. 1 shows a side and front view of the Joubert BB2 submarine and the coordinate systems used in the paper. Table .1 shows the full and model scale geometric main parameters of the Joubert BB2 used in this paper, and the scaling ratio equals 18.348 which is consistent with international conventions and facilitates subsequent comparison of resistance results.

3. Numerical methods

3.1. Governing equations

In this paper, the main objective is to simulate the free surface signatures of a submarine in the linearly stratified fluid. Based on an approach similar to Chung and Matheou (2012), we solve the Navier-Stokes equations under Boussinesq approximation and propose a thermocline model to achieve the density stratified fluid. The whole process is implemented in the commercial software Simcenter STAR-CCM+ framework Cao et al. (2021). The continuity, momentum, and heat equations are shown as below:

$$\nabla \cdot \boldsymbol{u} = 0 \tag{3}$$

$$\frac{\partial \boldsymbol{u}}{\partial t} + (\boldsymbol{u} \cdot \nabla)\boldsymbol{u} = -\frac{1}{\rho}\nabla P + \upsilon \nabla^2 \boldsymbol{u} + \beta \boldsymbol{g} T' + \boldsymbol{f} \tag{4}$$

$$\frac{\partial T'}{\partial t} + (\boldsymbol{u} \cdot \nabla)T' + \gamma u_z = \alpha \nabla^2 T' \tag{5}$$

note that heat equation (5) is a deformation of the energy conservation equation and where $\boldsymbol{u}$, ρ, P, υ, α, β, $\boldsymbol{g}$, T', $\boldsymbol{f}$ denote the velocity, density, modified pressure, kinematic viscosity, thermal diffusivity, volumetric expansion coefficient, gravitational acceleration, temperature fluctuation, and large-scale force required to maintain the turbulence, respectively.

3.2. The thermocline model

Pycnocline generally refers to density, but the corresponding nomenclature can be alternatively used to indicate a change due to salinity (halocline) or temperature (thermocline). In the open sea, the variation of salinity can be ignored when referring to temperature fluctuation. Therefore, in this paper, we mainly focus on the thermocline, which means that density can be simply specified as a function of temperature.

Firstly, based on Spedding (2014), for the top 40–500 m of the sea, we can describe density ρ as a function of temperature T in the form of a polynomial expression while the temperature ranges as a function of the depth z below the free surface in the first step.

Then, in the second step, the density ρ and temperature T can be written as follows:

$$\begin{cases} T = f(z) = T_0 + c_1 \cdot z \\ \rho = \rho(z) = g(z) = \rho_0 - c_2 \cdot z \end{cases} \tag{6}$$

where T_0, ρ_0 are the reference temperature and density, c_1 and c_2 are the temperature and density gradient, respectively.

In the third step, we establish a relationship between the density ρ and temperature T, and implement it within the physical models of STAR-CCM+ software. At the last step, Eqn. (6) and Eqns. (3)–(5) are solved together to achieve the linear stratification background in the flow field simulation.

3.3. Turbulence modeling

The whole problem is simulated with Reynolds averaged Navier-Stokes (RANS) equation, and the Shear-Stress Transport (SST) k-ω turbulence model is adopted to close the equation. The governing equations of k and ω can be written as follows.

$$\frac{\partial}{\partial t}(\rho k) + \nabla \cdot (\rho \boldsymbol{v} k) = \nabla \cdot \left(\mu_{eff,k} \nabla k\right) + \underbrace{P_k - \beta^* \rho k \omega}_{S^k} \tag{7}$$

$$\frac{\partial}{\partial t}(\rho \omega) + \nabla \cdot (\rho \boldsymbol{v} \omega) = \nabla \cdot \left(\mu_{eff,\omega} \nabla \omega\right) + \underbrace{\widetilde{C}_\alpha \frac{\omega}{k} P_k - \widetilde{C}_\beta \rho \omega^2 + 2(1 - F_1)\sigma_{\omega 2} \frac{\rho}{\omega} \nabla k \cdot \nabla \omega}_{S^\omega} \tag{8}$$

where all their coefficients depend on the Menter and Kuntz (2004).

3.4. The volume of fluid method

The volume of fluid (VOF) multiphase model is adopted in this paper (Hirt and Nichols, 1981). Depending on the different values of the volume fraction q we can distinguish the position of the interface:

- $q = 0$ the cell is completely void of phase air;
- $q = 1$ the cell is completely filled with phase water;
- $0 < q < 1$ indicate the presence of an interface between air and water.

4. Computational setup and validation

4.1. Computational domain and discretized mesh

The computational domain is a cuboid with the submarine place at the front of the block. To reveal the main characteristics of the flow

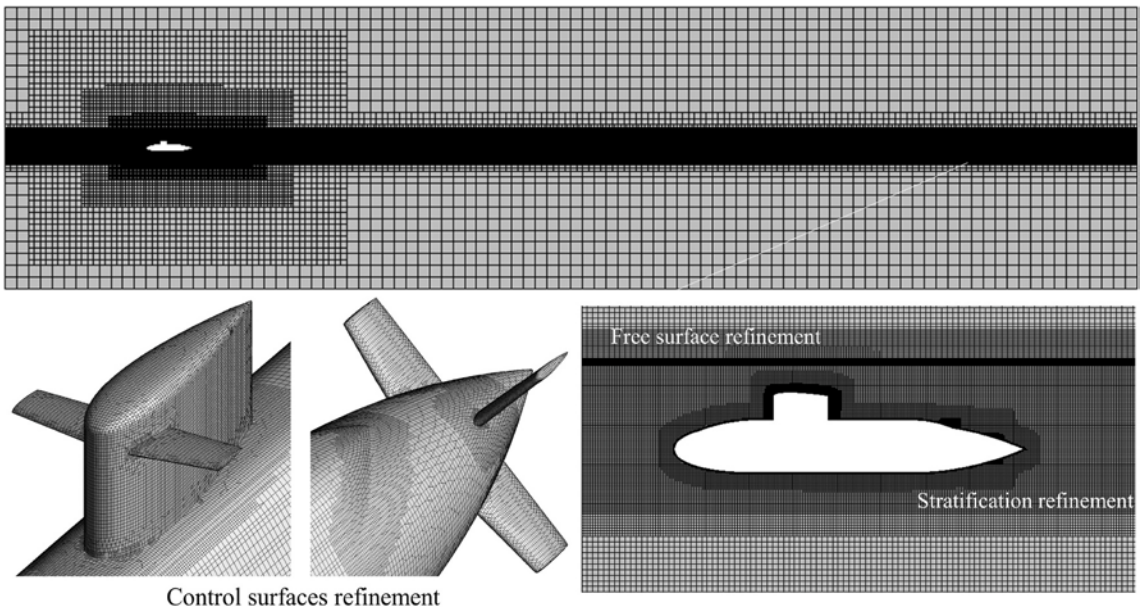

Fig. 3. Computational grids for the Joubert BB2 submarine with grids details on the main BB2 submarine control surfaces.

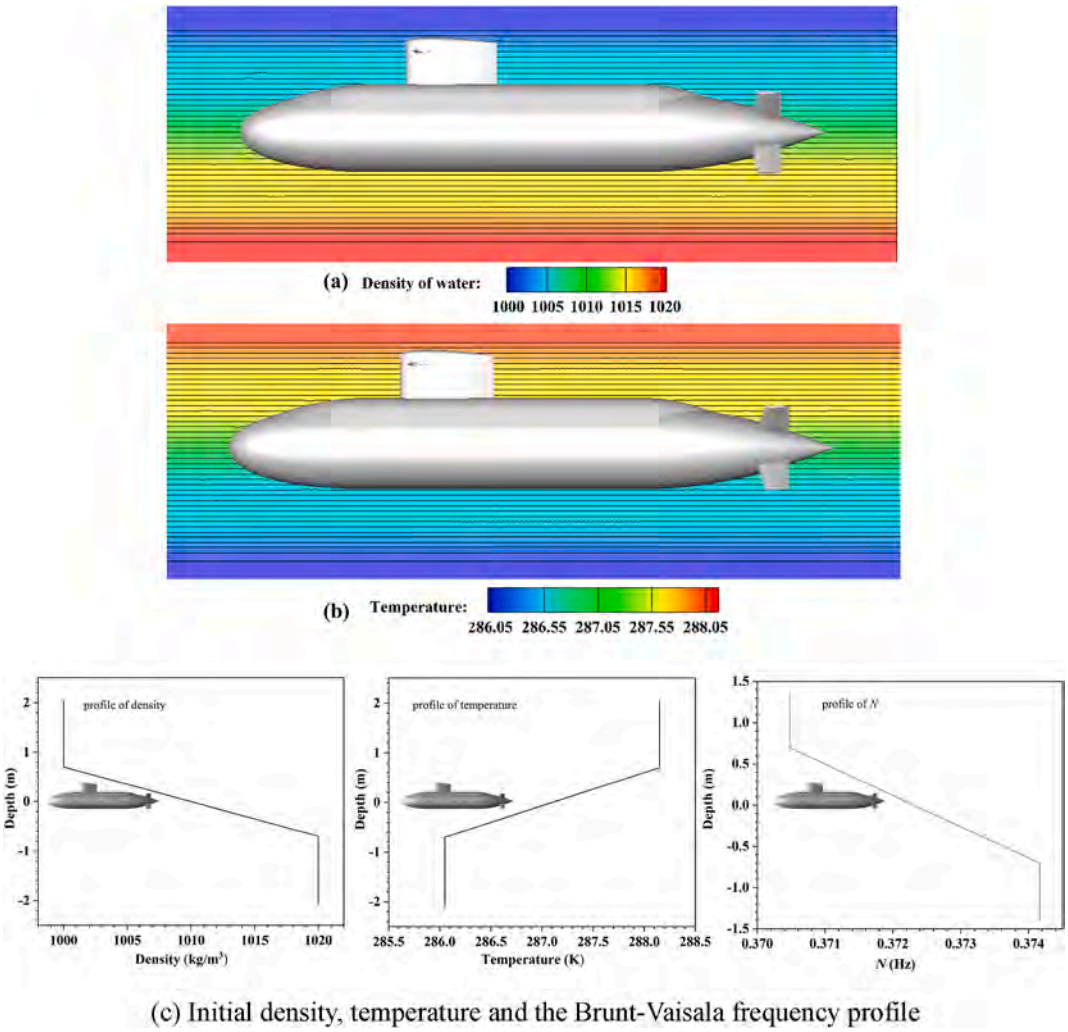

Fig. 4. Initial density, temperature and the Brunt-Vaisala frequency profile.

Table 2
Series of grids used in mesh convergence studies.

Cases	Coarse	Fine
Homogeneous	3.5million	10 million
Stratified	5.7 million	16 million

Table 3
Summary of mesh convergence studies in normalized resistance coefficient.

Normalized resistance coefficient ($X'\cdot10^3$)	Coarse	Fine	Difference
Homogeneous	1.81	1.82	0.55%
Stratified	1.94	1.92	1.04%

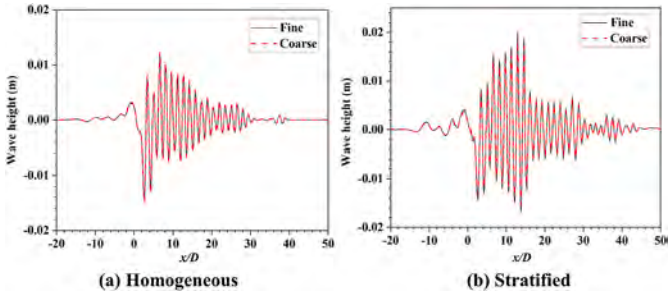

Fig. 5. Free surface profiles compared the Fine and Coarse at a special x-z slice ($y = 0$).

Table 4
Comparison of the BB2 forces and moments in deeply submerged conditions.

Simulation Type	$Re\cdot10^{-6}$	$X'\cdot10^3$	$Z'\cdot10^4$	$M'\cdot10^4$
STAR-CCM+ – SST (Present)	4.6	1.82	1.16	0.79
ReFRESCO – KSKL (Torunski, 2016)	4.6	1.83	1.24	0.99
ANSYS CFX – SST (Bettle, 2020)	3.9	1.87	1.06	1.03
STAR-CCM+ – SST (Donadei, 2019)	3.9	1.85	1.13	1.04

B. Free surface characteristics.

downstream, the whole domain extends to 4L in front of the submarine, 20L behind the submarine, and 7L in each broadside. The vertical dimension of the simulation is set to 3L to avoid wall effects. The computational domain size used in this study is much larger than the required domain size for flow past a submarine reported in previous studies. In order to avoid waves reflection, a sponge layer with length of 1L is introduced in the inlet and broadside. Besides, four types of boundary conditions are implemented in this paper. A no-slip wall boundary condition is set for the Joubert BB2 submarine; velocity inflow and outflow boundary conditions are applied for the inlet and outlet, respectively, and a symmetry boundary condition on the rest of the domain. Fig. 2 helps to visualize the dimensions listed above.

Fig. 3 shows the entire computation grid for the whole domain. A half mesh with a symmetry plane $y = 0$ is initially created. It is then mirrored. More cells are added in the port, starboard, rudder, and stern areas to ensure the proper resolution of the shear layer to reduce force and moment errors. During the simulation, the minimum cell thickness from the hull is 1×10^{-4} m, the boundary layers are set as 12, the y^+ is constantly kept between 30 and 100, and the time step is set as $\Delta t = 5 \times 10^{-3}$s. Additionally, the refinements of the key zones like stratification and the free surface parts are well maintained to guarantee a stable solution and capture differences between the stratified and unstratified cases. The density of the water ρ can be expressed as a function of temperature T which will be described carefully in section 4.2. The total

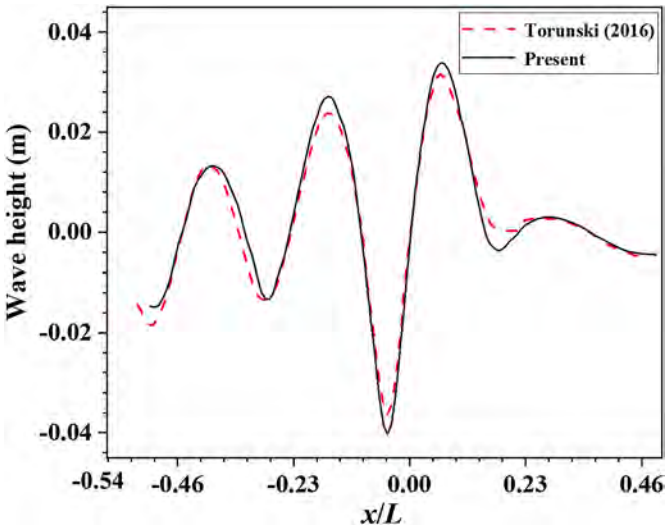

Fig. 7. Comparison of the free surface wave height of a special x-z slice ($y = 0$) between Torunski (2016) and the present.

Table 5
Normalized resistance coefficient X' for homogeneous and stratified cases.

Normalized resistance coefficient	Homogeneous	Stratified	Difference
$X'\cdot10^3$	1.82	1.92	+5.5%

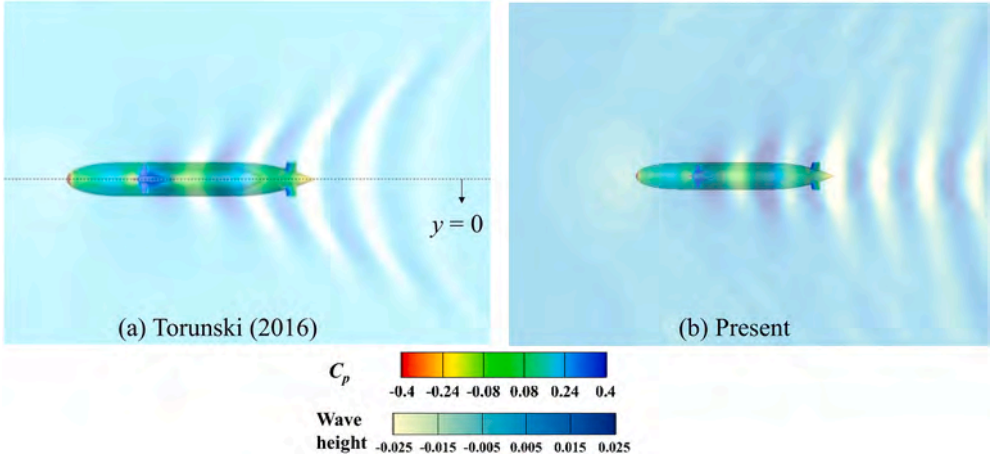

Fig. 6. Comparison of the steady-state free surface profiles at a certain depth $z = 0.205L$ between Torunski (2016) and the present.

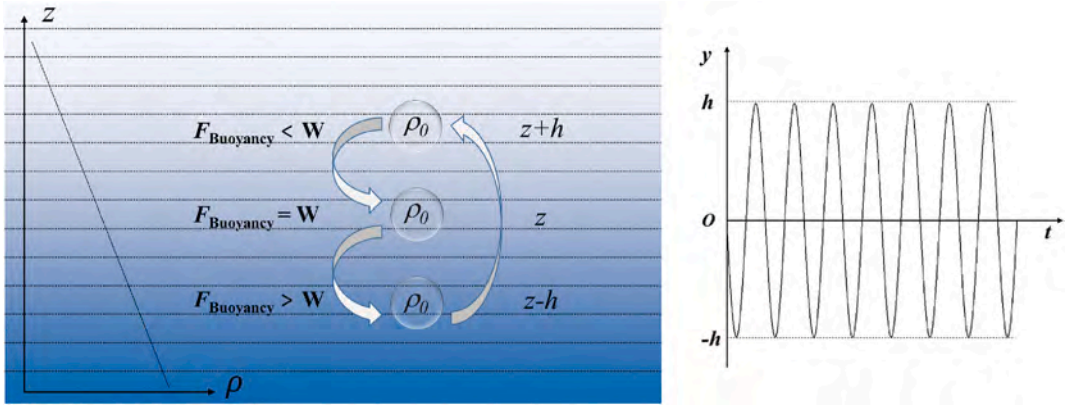

Fig. 8. A fluid particle is placing in the linearly stratified environment ($y = 0$).

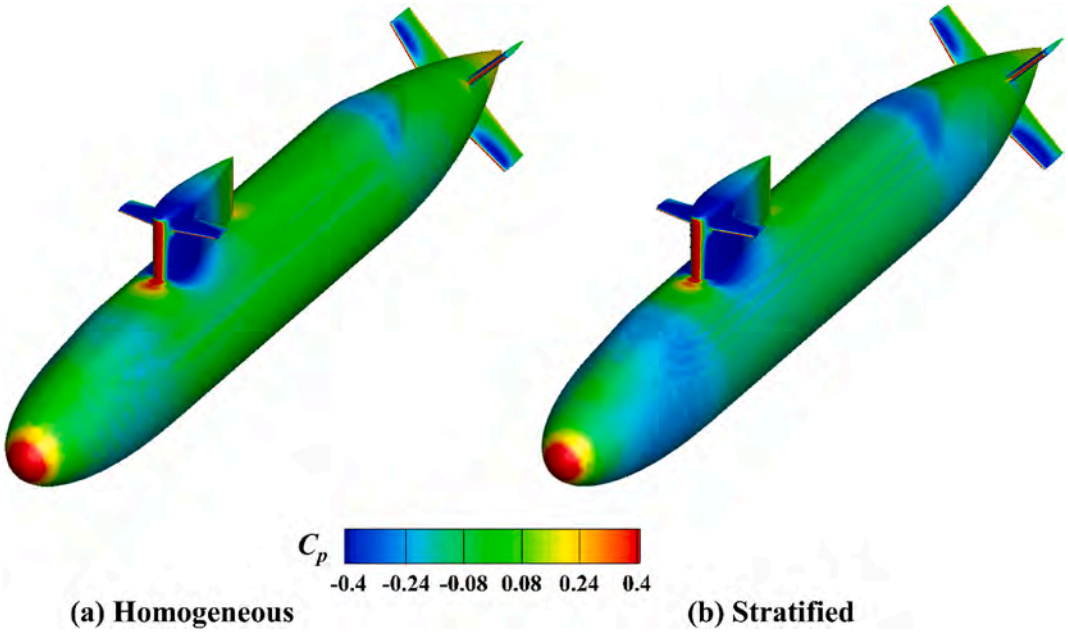

Fig. 9. The pressure distribution on the submarine surface.

number of cells is about 10 million and 16 million for the homogeneous and the stratified, respectively.

4.2. Initial conditions for the stratification simulation

In this paper, all cases are performed at a model scale submarine model with all appendages near the free surface ($z = 0.25L$) with an onset velocity of $U = 1.201$ m/s. As to the stratified case, we simulate a weakly stratified condition with $Fr \approx 3$. The linear density stratification visualized in Fig. 4 can be specified as a function of temperature in the form of a polynomial expression described in Eqn. (6). While the temperature is a function of depth z, which is measured from the submarine to the calm water surface. As depicted in Fig. 4, $T_0 = 287.1$ K and varies from 288.15 K to 286.05 K at the top and bottom, and $\rho_0 = 1010$ kg/m^3 and varies from 1000 kg/m^3 to 1020 kg/m^3. Here, we set the higher temperature on the sea surface as 288.15 K which is consistent with the annual average temperature in east China sea, and the temperature gradient $\Delta T/\Delta z$ equal to 1.5 °C/m which is consistent with the strongest temperature gradient in the offshore east China sea. Accordingly, the density on the sea surface is 1000 kg/m^3 which is a common sense for freshwater, and we also set the density gradient $\Delta\rho/\Delta z$ greater than 0.5kg/m^{-4} to reflect the real conditions of the east China sea. Moreover, in this paper, we only chose $Fr \approx 3$ to represent the common stratification level of the east China sea. Fig. 4 helps to visualize the initial conditions set for the stratified case located at the median vertical plane ($y = 0$). Fig. 4(a) shows the initial density distribution, Fig. 4(b) displays the initial temperature distribution, and Fig. 4(c) gives the density and temperature profile after the flow field initiation.

4.3. Mesh convergence studies

Convergence studies are carried out to determine the proper grid sizes of the simulations. The grid convergence computations are performed both in the homogeneous case and the stratified case. There are two series of grids named Coarse and Fine grid, respectively. It should be noted that the researches are based on a fine grid that contains 10 million and 16 million cells and a coarse grid that contains 3.5million and 5.7 million cells, respectively. The grid refinement ratio is $r_G = \sqrt{2}$.

The procedure of analyzing the mesh convergence studies is applied to the straight flow cases while the normalized force X' represents the resistance coefficient and the free surface wave height of a special x-z slice ($y = 0$) are selected to be compared respectively. Table .3 shows the summary of mesh convergence studies in normalized resistance coefficient. As can be seen in Table .3, the total difference between Corase and

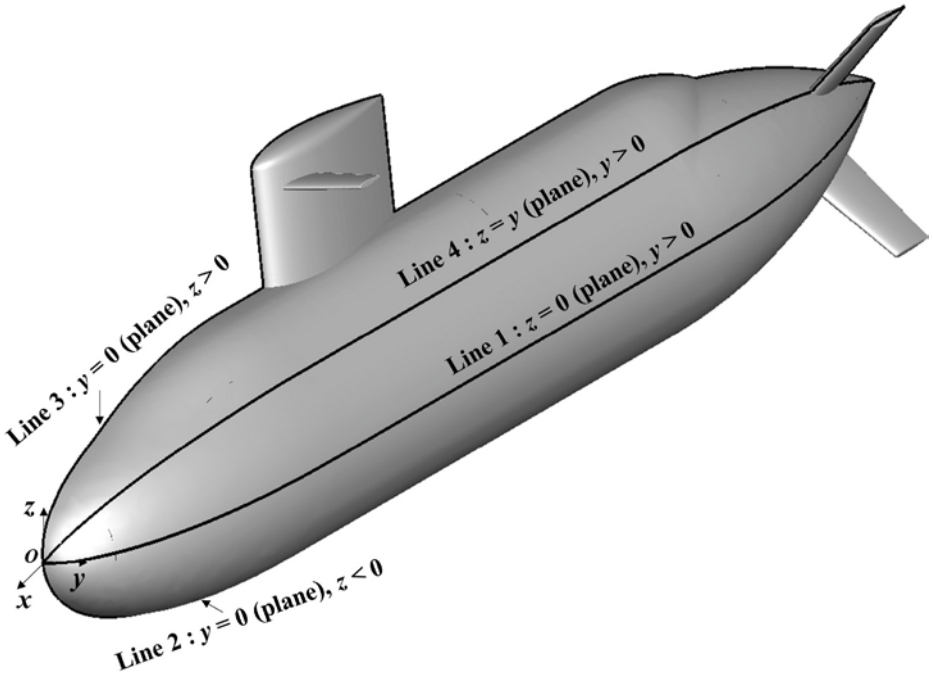

Fig. 10. The position of the selected three special azimuthal planes.

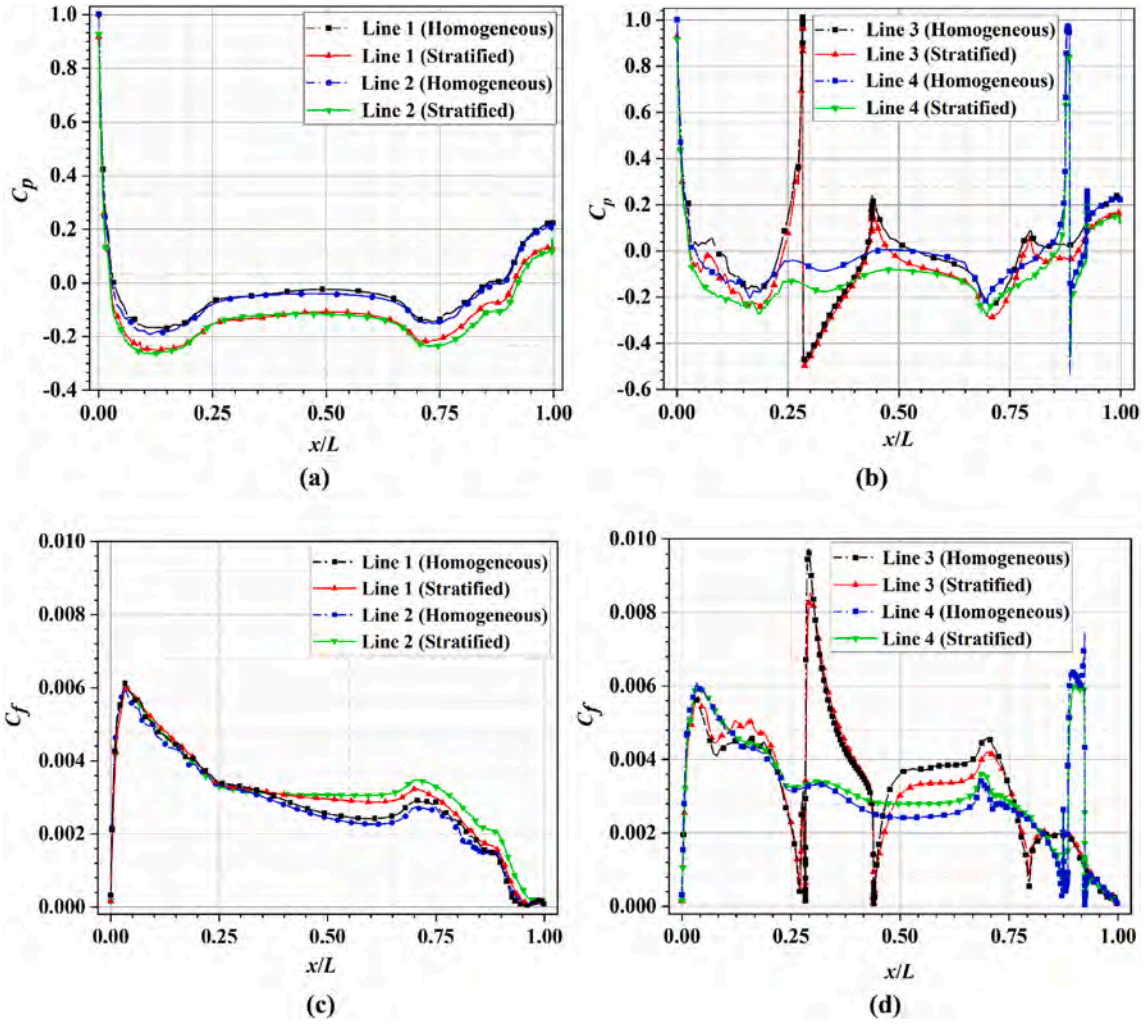

Fig. 11. Time-averaged distributions of (a), (b) pressure coefficient; (c), (d) skin-friction coefficient at different locations along the submarine surface.

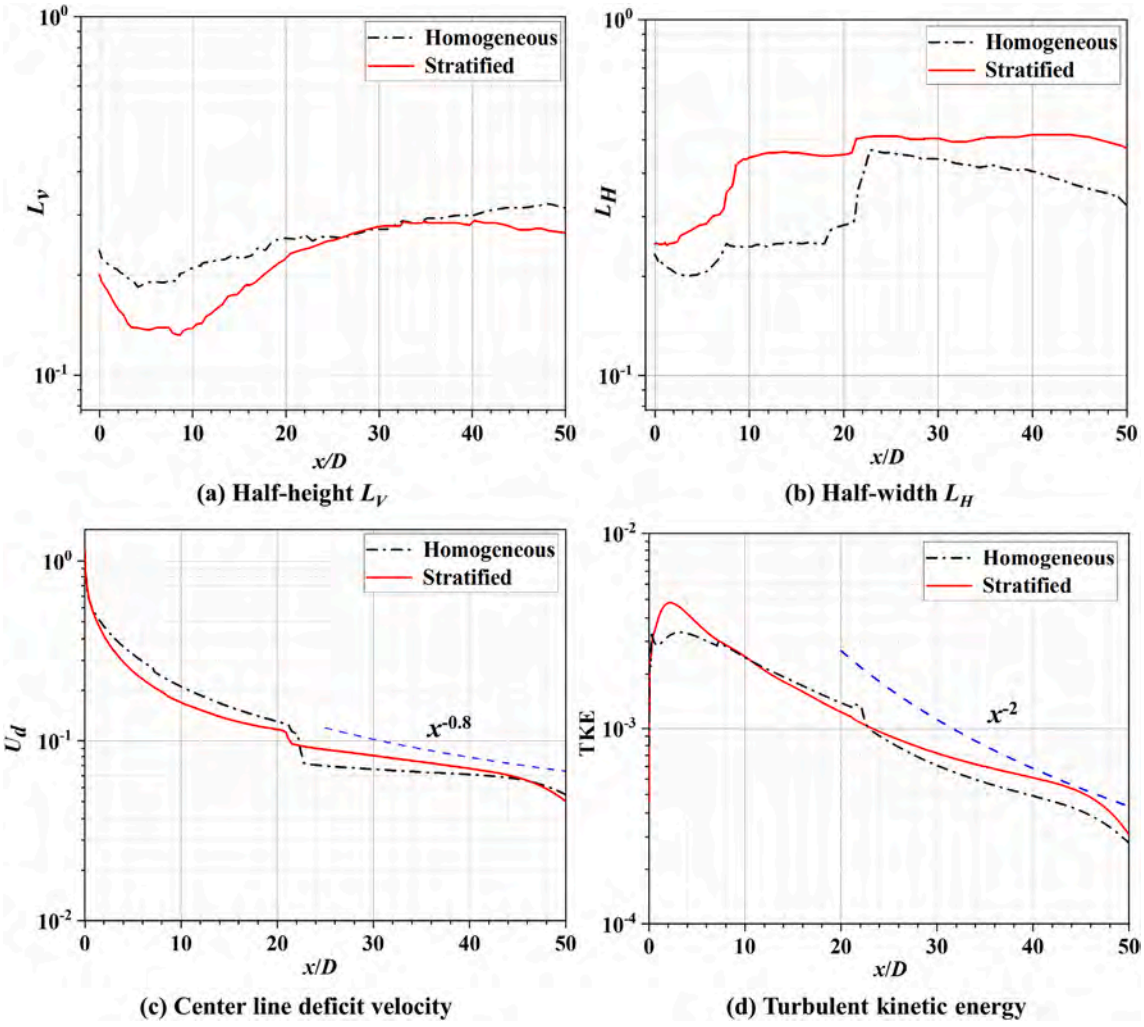

Fig. 12. Effect of stratification on the streamwise evolution of overall wake properties.

Fine grids only amounted to 1%. Fig. 5 shows the free surface profiles compared the Fine and Coarse at a special *x*-*z* slice ($y = 0$). The black solid line stands for the Fine grid, and the red dash line represents the Coarse grid. These graphs verify the Fine grid results are convergent.

4.4. Solution validation

Regarding the validation of the thermocline model in this paper, our team have already analyzed the cylinder in stratified flow in a published paper by Ma et al. (2018). In the previous study, a cylinder in the stratified environment which is consistent with the experimental conditions of Boyer et al. (1989) were numerically investigated. Both the high and low *Fr* conditions were performed. The paper showed that the numerical results agreed well with the experimental results. Besides the *Fr*, the influence of the *Re* and turbulence models were also tested. Results showed that the thermocline model we used can accurately capture the flow field details and turbulent wakes.

Due to the lack of stratified data for submarine, the validation study is conducted only for the homogeneous case. This procedure chose the same parameters as Torunski (2016), all cases are performed near the free surface ($z = 0.205L$). This part is aimed to gain further confidence in the CFD results and ensure a proper grid size and resolution are used to capture the correct characteristics of the free surface.

4.4.1. Forces and moments

Table .4 shows the analyzed results of the submarine hydrodynamic data is deeply submerged conditions. Using Eqn. (9) and Eqn. (10), forces (X, Y, Z) and moments (K, M, N) are made non-dimensional for easy comparison. The normalized force X' represents the resistance coefficient, positive Z' here shows an attempting to push the submarine to the surface, and M' is the non-dimensional pitch moment which equals positive indicating a bow-up moment. Current results have been compared with other results obtained by different CFD solvers and turbulence models with a good agreement. As Table .2 suggests, there is only a weak Reynolds number dependence in the non-dimensional force and moment value for all simulations conducted. Results in this paper show a slightly smaller resistance force and pitch moment than the previous simulation. A 0.55% difference in X' was found between the current results and Torunski (2016), while a 6.45% and 20.2% difference was found for Z' and M', respectively. The resistance and pitch moment also show good agreement with the additional data obtained by Bettle (2020) and Donadei (2019), at a Reynolds number of 3.9×10^6.

$$X', Y', Z' = \frac{X, Y, Z}{\frac{1}{2}\rho U^2 L^2} \tag{9}$$

$$K', M', N' = \frac{K, M, N}{\frac{1}{2}\rho U^2 L^3} \tag{10}$$

where ρ is fluid density, U is the submarine speed, and L is the length of the submarine.

Since the following part involves the analysis of the free surface characteristics, the "wiggles" in the free surface can be influenced by the

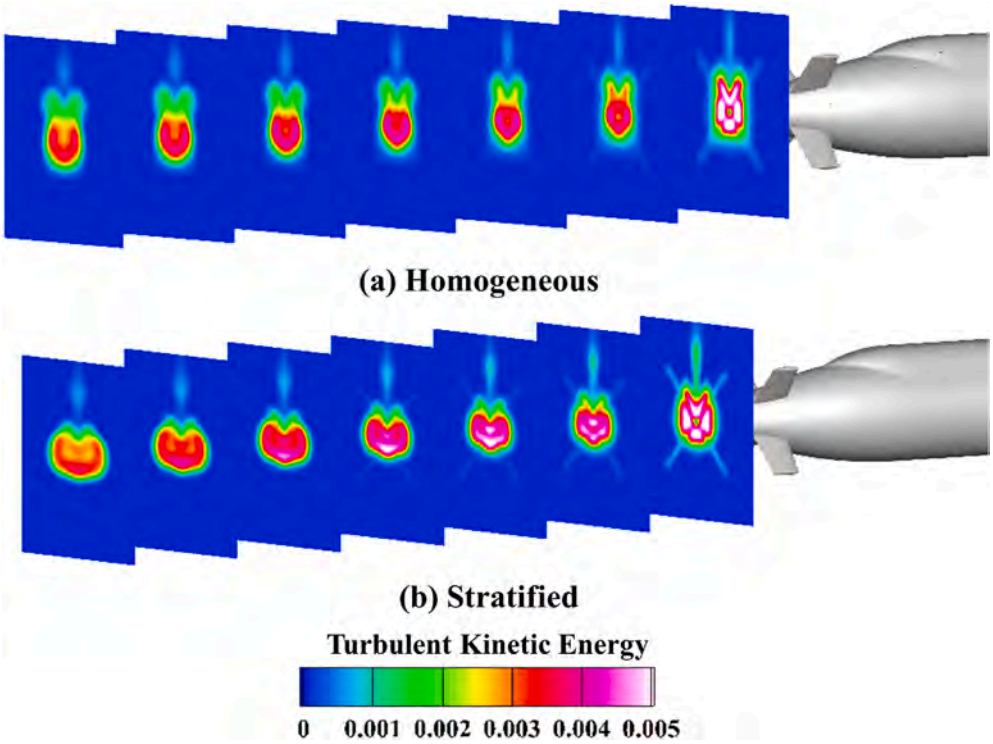

Fig. 13. Turbulent kinetic energy fields at seven stations downstream.

free surface model, grid size, and the use of far-field damping. In order to test which settings and grids provided the best results, a comparison of the free surface simulation results between current and reference has been conducted.

As shown in Fig. 6, we compared the steady-state free surface profiles at a certain depth $z = 0.205L$ with the reference. Potential flow theory suggests that, for a vessel far above the ocean floor, the submarine body should produce a Kelvin wedge of 19.47°. The present result shows the Kelvin wedge of 19.5° on the free surface. Obviously, the current method can capture free surface characteristics correctly and closely match the theoretical value. Moreover, we compare the free surface wave height of a special x-z slice located at $y = 0$ as depicted in Fig. 6 (a). In Fig. 7, the red dash line represents Torunski (2016) result, and the black line marks the current result. The value 0.46 corresponds to the bow of the submarine, and −0.54 corresponds to the stern of the submarine. The free surface wave height of a special x-z slice ($y = 0$) has also been compared with Torunski (2016), which also shows an excellent agreement.

5. Results and discussions

In this part, four main aspects are chosen to discuss the specialty of stratified fluid by comparing the drag force, downstream wakes, internal waves, and free surface signatures with that of the homogeneous one.

5.1. Drag force enhancement

Table .5 shows the normalized resistance coefficient X' for the homogeneous and stratified cases. It is evident that the stratified case has a slightly larger resistance force than the homogeneous one. As Table .5 indicates that there is about a 5.5% increase between the stratified and unstratified cases. This phenomenon normally occurs in the stratified fluid. Srdić-Mitrović et al. (1999) carried out a detailed experimental study to investigate the settling of solid spherical particles through density interfaces. He recorded that the drag coefficient could be an order of magnitude larger than its homogeneous-fluid counterpart. Moreover, Torres et al. (2000) reported that the drag force increase, especially at a very low Froude number ($Fr \leq 1$) when the flows are generated by a sphere moving in a uniformly stratified fluid. It is interesting that even in the horizontal weakly stratified environment, the drag force enhancement phenomenon still exists.

The mechanism of the drag force enhancement can be explained as follows. As shown in Fig. 8, let us assume that the stratification comprises many thin layers with slightly different densities. We consider a particle with volume V and density ρ_0 at the elevation z to be balanced where gravity and buoyancy are equal. If a vertical pulsating force pushes the particle to move in the negative direction, we assume that the particle will move downwards to the elevation z-h. At this point, the particle is surrounded by heavier fluid so that the buoyant force is larger than the weight of the particle. Then the particle rises, it overshoots the original position z though. The particle moves to the elevation z+h, where the buoyant force is smaller than the gravity. The particle will move downwards due to the imbalances of gravity and buoyancy. As a result, the fluid particle oscillates with a natural frequency N illustrated in Fig. 8.

Once the buoyancy effect works, the vertical velocity will increase, converting the potential energy to vertical kinetic energy. Because of the extra energy conversion, submarines in the stratified fluid need more energy to attain the same speed in the unstratified flow, which manifests as an increase in resistance. On the other hand, the motion of the submarine in the stratified environment will generate internal waves. According to Torres et al. (2000), the internal wave-making resistance is analogous to the free surface wave-making resistance, resulting in a force several times higher than that of a vessel sailing in non-stratified waters. Thus, internal waves generated by the moving submarine are another reason for the increase in drag force. Henceforth, the reasons for drag force enhancement can be briefly concluded as flow structure modification around the hull due to the density gradient and internal waves.

5.2. Frictional drag and pressure coefficients

To better understand the effect of stratification on drag forces, it is

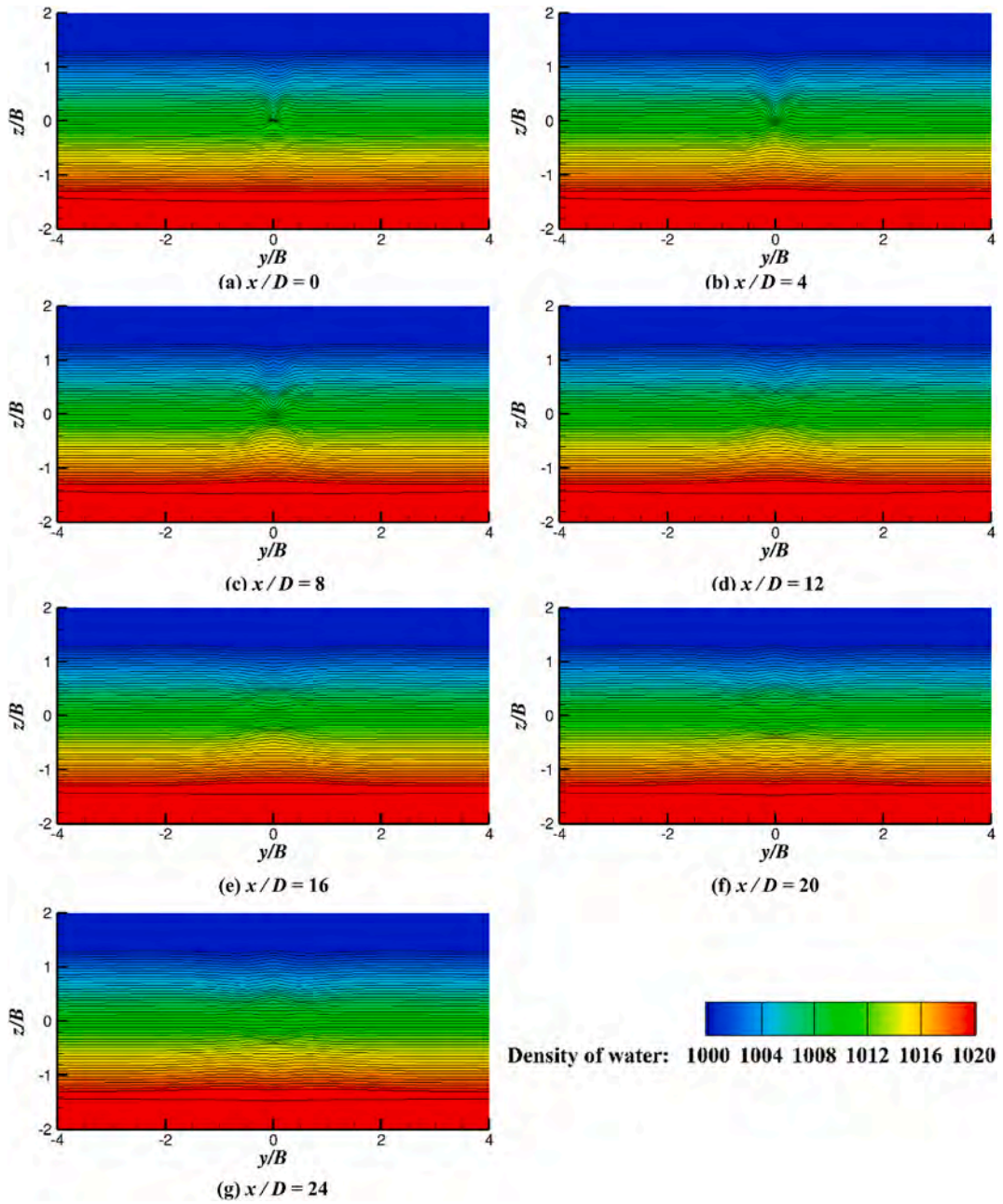

Fig. 14. Density fluctuations in seven different locations.

helpful to look at the streamwise evolution of the frictional drag coefficient C_f and pressure coefficient C_p, respectively. The skin-friction coefficient C_f and the pressure coefficient C_p are obtained by Eqn. (11) and Eqn. (12), respectively.

$$C_f = \frac{\tau_w}{\frac{1}{2}\rho_h U^2} \tag{11}$$

$$C_p = \frac{P - P_h}{\frac{1}{2}\rho_h U^2} \tag{12}$$

where τ_w is the wall stress. In the stratified case, ρ_h is changed with different layers, while in the homogeneous case, ρ_h is treated as a constant 998 kg/m^3. P_h corresponds to the free-stream pressure at different position z and is calculated using

$$P_h = \rho_h g z \tag{13}$$

The pressure distributions on the submarine surface are shown in Fig. 9. There are high-pressure areas on the bow of the submarine both in the homogeneous and stratified cases, which indicates the areas of high drag. Moreover, the pressure distribution on the submarine surface in the forward and rearward portions differs between these two cases.

Four different lines are on these three special azimuthal planes are selected to discuss these two coefficients in detail, as depicted in Fig. 10. Because of the presence of appendages, the symmetry around the axis is lost, the evolution of the pressure and skin-friction coefficients are different on different azimuthal planes. The selection principle of four different lines is simple, Line.1: [$z = 0$ (plane), $y > 0$] and Line.2: [$y = 0$ (plane), $z < 0$] are located on the hull ignoring the influence of appendages to the greatest extent, and Line.3: [$y = 0$ (plane), $z > 0$] and Line.4: [$z = y$ (plane), $y > 0$] are chosen to illuminate the effect of both sail and stern appendages.

Firstly, from Fig. 11 (a), we investigate the distribution of pressure coefficient on the hull ignoring the influence of appendages. Line.1 and

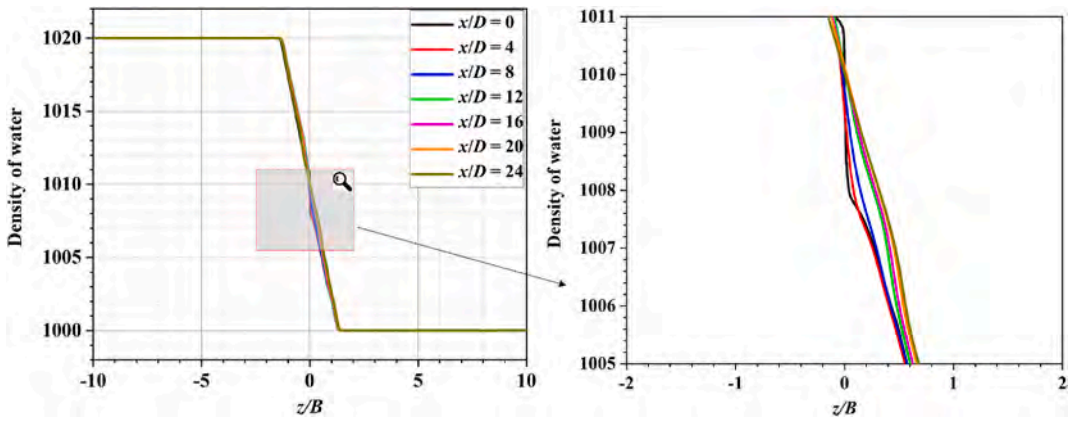

Fig. 15. Density fluctuation of lines at different locations.

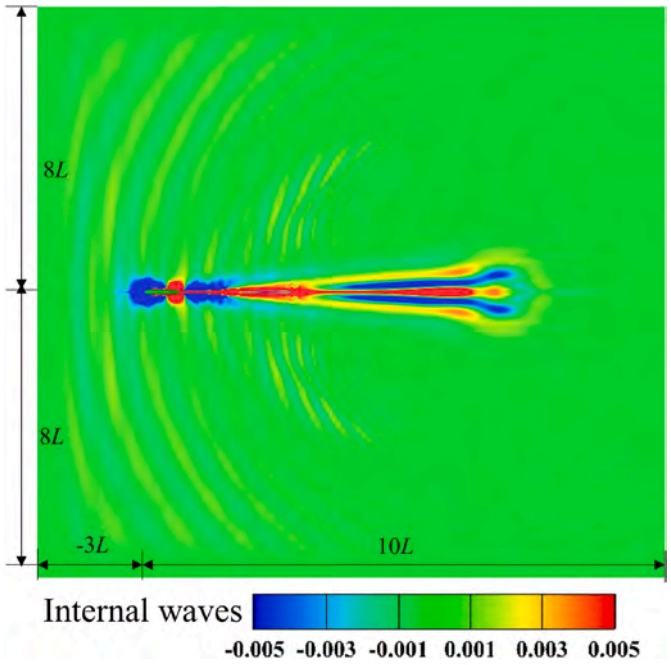

Fig. 16. The contour of internal waves (divergence field Δz) in a plane of $z = 0$.

Line.2 show the same trend. The bow of the submarine has a stagnation point where the flow kinetic energy is converted into pressure, which also explains the area of high pressure on the bow of the submarine in Fig. 9. During its motion towards the submarine ($0 < x/L < 0.7$), the fluid accelerates, and the kinetic energy recovers at the expense of pressure drop. However, in the downstream ($0.7 < x/L < 1.0$), the behavior is reversed, velocity decreases, and pressure rises again. Noting there are some fluctuations on the curves, since the junction vortices originated at the root of appendages and bring higher momentum fluid. By comparing the stratified and homogeneous cases, the pressure in the forward portion ($0 < x/L < 0.7$) increases relative to the homogeneous case, while the flow reaches downstream ($0.7 < x/L < 1.0$), the behavior is reversed. Because of the effect of viscous losses (Ortiz-Tarin et al., 2019), the recovery of pressure to be partial in the stratified case, which would be readily understood the decrease C_p on the rearward portion relative to the unstratified counterpart. Moreover, in the nose of the bow ($0 < x/L < 0.05$), the pressure drops quickly, the body-tangential component of the gravity vector and the buoyancy term in the momentum conservation equation reduce the flow speed so that the pressure increases in the forward portion compared to the homogeneous case.

Secondly, Fig. 11 (c) shows the skin friction coefficient at different locations along the submarine surface. The reduction of flow speed in the bow leads to a smaller value of C_f, whereas the enhanced flow speed on the rearward portion increases the skin friction. Finally, Fig. 11 (b) and (d) aim to elucidate the effect of appendages. Although the presence of appendages, trends turn to be the same as Fig. 11 (a) and (c). Thus, we can conclude that stratification increases the drag primarily by reducing the overall pressure in the rearward portion and increasing the pressure in the forward portion, which is consistent with a prolate spheroid simulation investigated by Ortiz-Tarin et al. (2019).

5.3. The evolution of wakes

Besides the drag force difference, stratification also affects the establishment of the wakes and their downstream evolution. This section discusses the structure and decay of the near wake by looking into its size and energy.

The downstream wake can be generally characterized by the centerline velocity deficit, $U_d = u - U$, and the magnitude of the half-thickness, including half-height L_V and half-width L_H. Note that the values L_V and L_H are estimated from the negative y and z of the Cartesian coordinate system and taken the absolute values. Typically values of U_d evolve according to a power law. For example, the decay of U_d for a sphere is close to $U_d \propto x^{-0.25}$ (Brucker and Sarkar, 2010).

Fig. 12 (a) and (b) discuss how buoyancy sets in to create anisotropy between L_V and L_H in stratified wakes. For the stratified case, the wake height saturates $L_V \approx 0.3$, while the maximum value of wake width fluctuates around 0.45, and further downstream, the growth of L_V and L_H reduces. The homogeneous case shows the same trend. The vertical wake thickness is compressed, and the horizontal wake width is expanded in the stratified flow, which is consistent with the explanation of drag force enhancement. The extra energy conversion in the vertical direction in the stratified fluid.

Fig. 12 (c) shows the evolution of the centerline velocity deficit U_d along the streamwise direction is around 50D distance. The decay rate exhibits the flattening trend, though a slight difference between the stratified and unstratified cases. Once buoyancy effects have set in, the value of U_d in the stratified wakes becomes more considerable than in homogeneous wakes. Thus, a "longer lifetime" wake in a stratified fluid is one of the remarkable features relative to the homogeneous fluid. The decay of U_d is close to $U_d \propto x^{-0.8}$, which is different from the previous findings for the sphere (Spedding, 1997), (Brucker and Sarkar, 2010). The difference between these near-field power laws is easy to understand since the shape of the geometry, and the Reynolds number chosen in this work is not small.

To vividly visualize the impact of the stratification on the turbulent behavior of the wake, Fig. 13 shows the evolution of turbulent kinetic

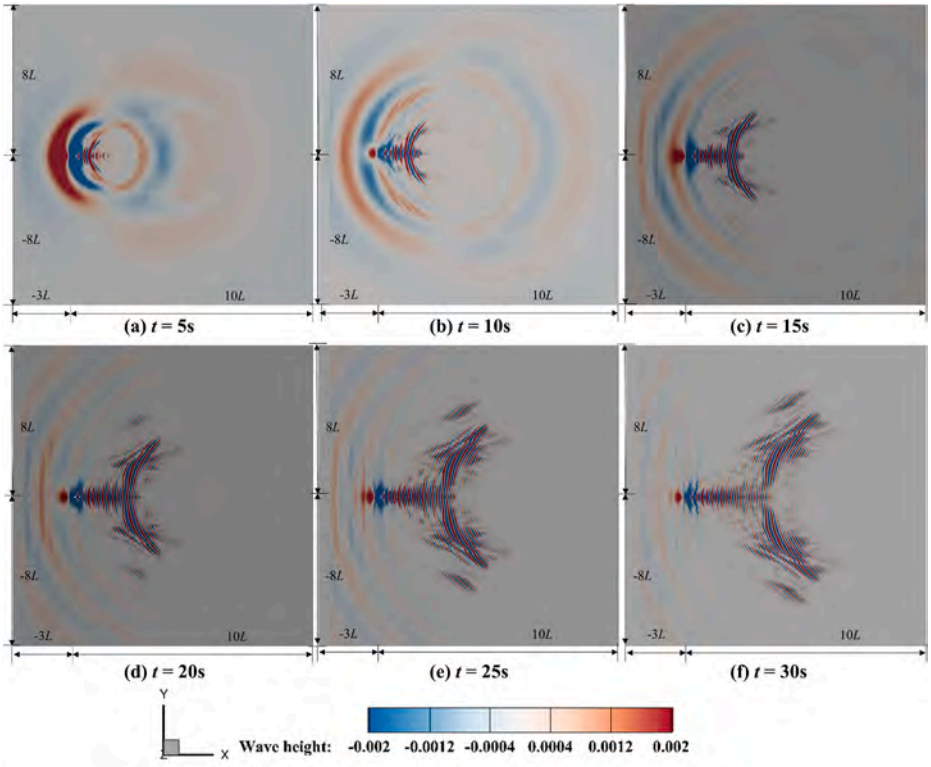

(a) Top view of wave profile in the homogeneous fluid

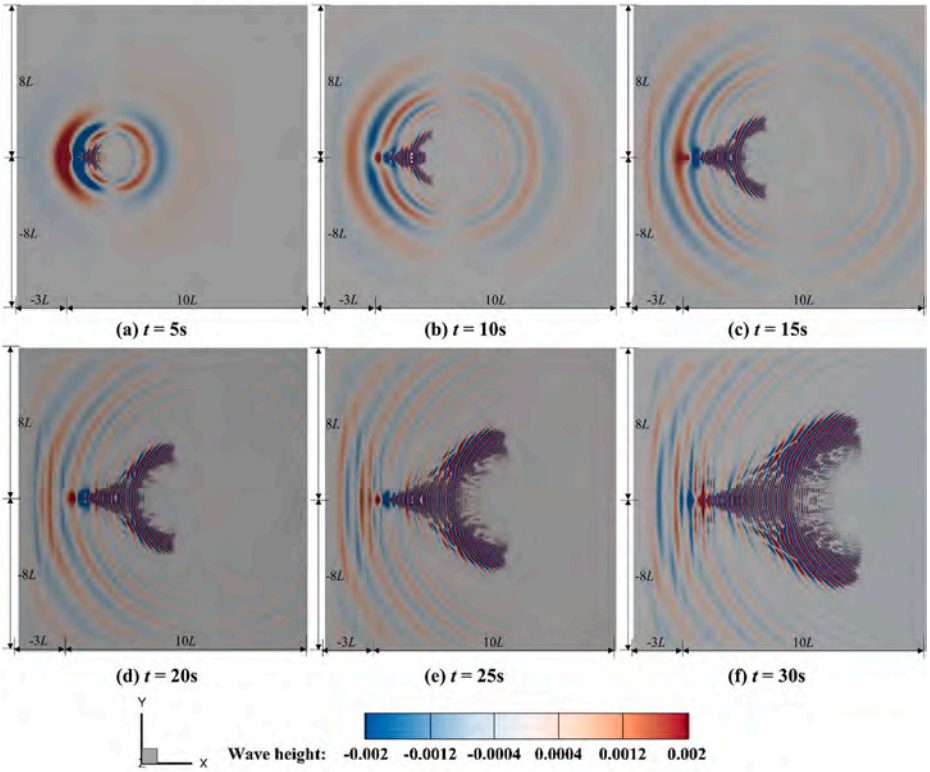

(b) Top view of wave profile in the stratified fluid

Fig. 17. Top view of the free surface profiles in the homogeneous fluid and stratified fluid, respectively.

energy (TKE) near the submarine at seven stations ($x/D = 1.0, 2.0, 3.0, 4.0, 5.0, 6.0, 7.0$), TKE is calculated by Eqn. (14). As mentioned before, in the stratified fluid, once the buoyancy effect works, the vertical velocity will increase, converting the potential energy to vertical kinetic energy. Thus, in the same station, such as $x/D = 2$, the value of TKE is bigger relative to the unstratified case. Moreover, due to the higher vertical velocity deficit in the stratified flow, the shape of downstream wake dyed by TKE turn to expand towards the y-direction. Fig. 12 (d)

Table 6
Free surface waveform characteristics between the homogeneous and stratified cases.

Description	Unit	Homogeneous	Stratified	Difference
Longitudinal propagation distance	m	63*D*	68*D*	+7.9%
Transverse propagation distance	m	38*D*	43*D*	+13.2%
The maximum wave trough value	m	0.0117	0.0206	+76.1%
The maximum wave crest value	m	0.0144	0.0174	+20.8%

shows a tendency of the centerline downstream TKE. In the stratified case, the TKE evolution shows a peak at $x \approx 2D$, while in the unstratified case, the peak shows a lag compared to the stratified case, the peak TKE is at $x \approx 3D$. The peak point is closer to the body for the stratified case since the vertical confinement by buoyancy in the stratified environment, and the velocity would decay slightly faster than the unstratified case.

$$K = \frac{1}{2}\overline{U_i U_i} \tag{14}$$

In the present simulation, we can conclude that stratified wakes have a wider influencing zone in the *x*-*y* plane than the unstratified case since the flow is vertically confined by stable stratification.

5.4. Density fluctuations and internal waves

The motions of a submarine in a stratified environment generate density fluctuation and internal waves. These waves are three-dimensional, dispersive, anisotropic, and emitted by multiple sources. It is essential to investigate these waves, which help us understand the effect of stratification on free surface waves.

The presence of the body distorts the originally stable horizontal isopycnals, mixing the fluids up and down over a distance much longer than the body size. To reveal the density fluctuations after the body, seven different downstream locations are chosen as Fig. 14 shows. These clips are located at $x/D = 0$, 4, 8, 12, 16, 20, 24, respectively. Due to the presence of the submarine, at $x/D = 0$, the stable isopycnals are distorted. The fluctuations between layers gradually decrease as the distance increases.

Moreover, in order to evaluate the degree of distortion downstream, we chose a specific line ($y = 0$) in each of the seven clips and drew a plot to analyze the density fluctuation of lines at different locations, as shown in Fig. 15. If we compared $x/D = 0$ and $x/D = 24$ at the same location $z/B = 0$, we would find that the density of water at the same height ($z/B = 0$) turns bigger, which should be originally equal. That means due to the motion of the submarine, the stable stratification has been destroyed, and the original layer's equal density has changed. The heavier water will gradually float up downstream contributing to the anisotropy of the wave height in the free surface as mentioned before. This also indicates that stratification will change the pattern of the free surface waves compared to the unstratified cases.

As for internal waves, according to Spedding (2014), the projection of the motions on horizontal plane $\{x, y\}$ gives estimates of the two horizontal velocity components, $\boldsymbol{q} = \{u, v\}$, and their gradient quantities ω_z and Δ_z. These two parameters are derived to reveal the nature of the flow. The magnitudes of the divergence field Δ_z are shown in Fig. 16 which can be regarded as approximately proportional to the amplitudes of vortex and wave motions in a plane of constant z, especially Δ_z can be used as an indicator of internal waves.

$$\Delta_z = \nabla \cdot \boldsymbol{q} \tag{15}$$

We chose a plane of constant $z = 0$ and dyed it by the divergence field Δ_z. After some time evolving, we can see that internal waves are emitted by the submarine. The coherent structures shed from the body and the

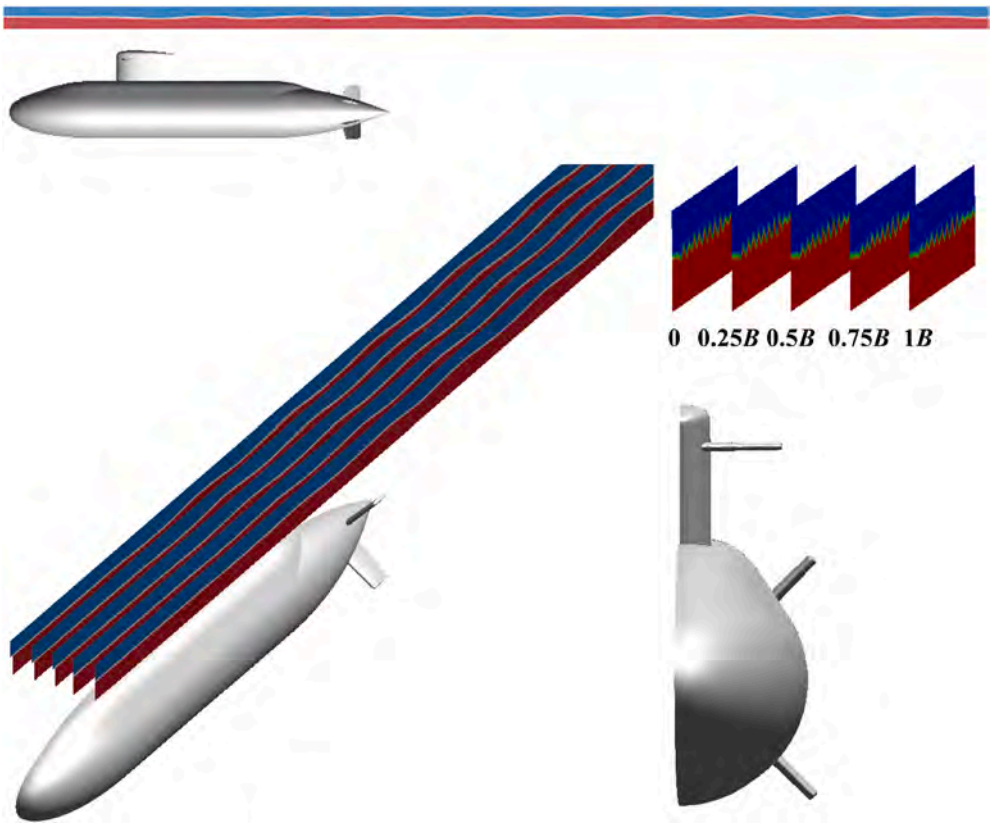

Fig. 18. Schematic diagram of five different *x*-*z* slices above the sail of the submarine at the location of the free surface.

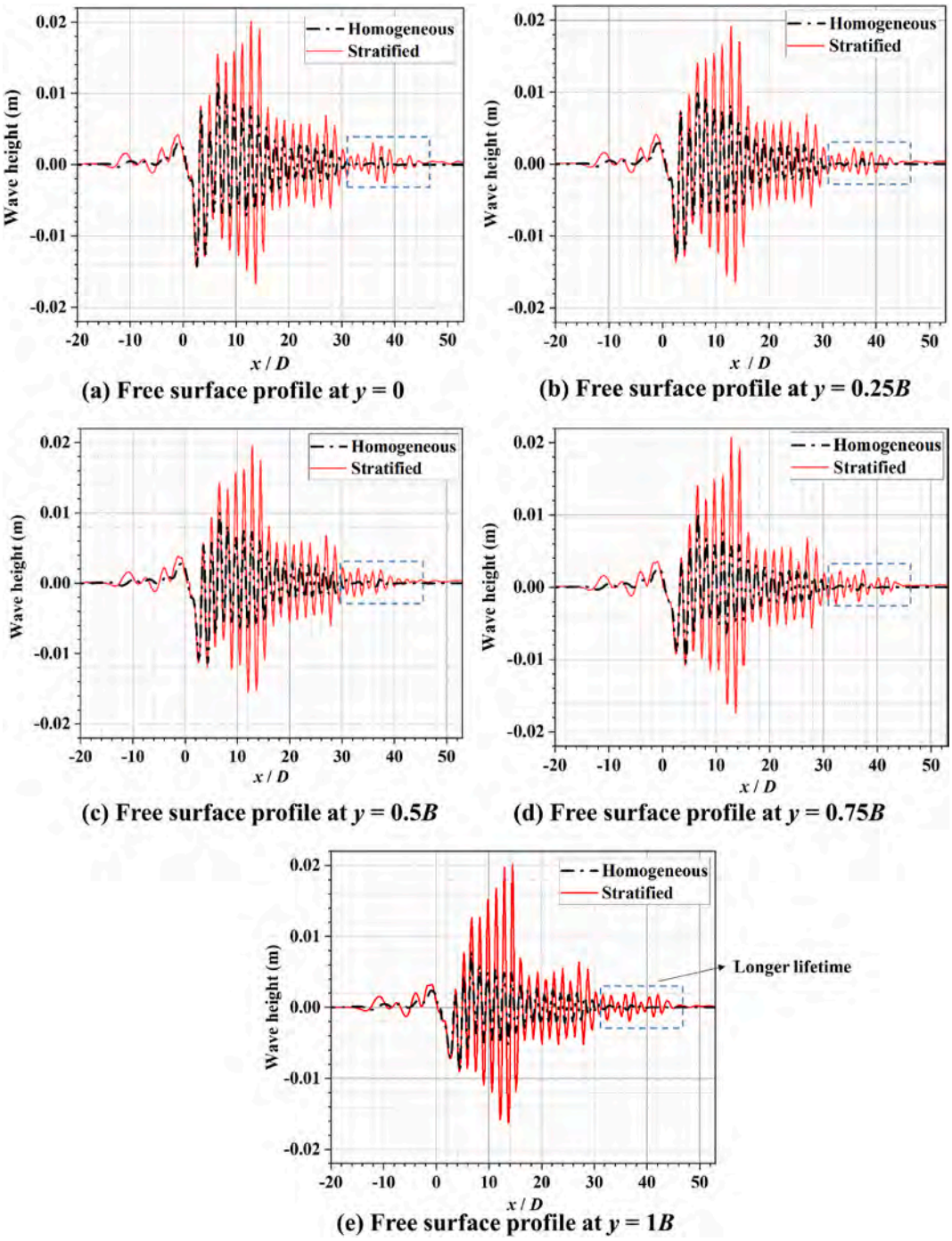

Fig. 19. Free surface profiles compared the homogeneous and stratified flow cases at various free surface depths. The black line represents the free surface height in the homogeneous fluid, and the red line marks the stratified fluid. (For interpretation of the references to colour in this figure legend, the reader is referred to the Web version of this article.)

downstream wake turbulence cause the internal waves exists for a long distance behind the submarine. Unlike the homogeneous case, these internal waves will change the wave patterns in the free surface which will carefully discuss in the following part.

5.5. Free surface waves

The internal waves and anisotropic turbulence produced by the moving submarine will change the surface roughness variations on the free surface, and these characteristics will be detected by the synthetic aperture radar. Detection of free surface wave signature induced by submarines in the stratified environment has been a canonical question. This section aims to elucidate the characteristics of waves on the free surface when operating submarine near-surface in the homogeneous and stratified fluid, respectively.

5.5.1. Free surface signatures visualization

When a submerged body displaces in the fluid, pressure variations around the body resulting in wave generation. This phenomenon can be seen in Fig. 17, where the waveform of the free surface in the homogeneous and stratified fluid over time are represented, respectively. The wave system in the surface-wave mode is made up of transverse waves

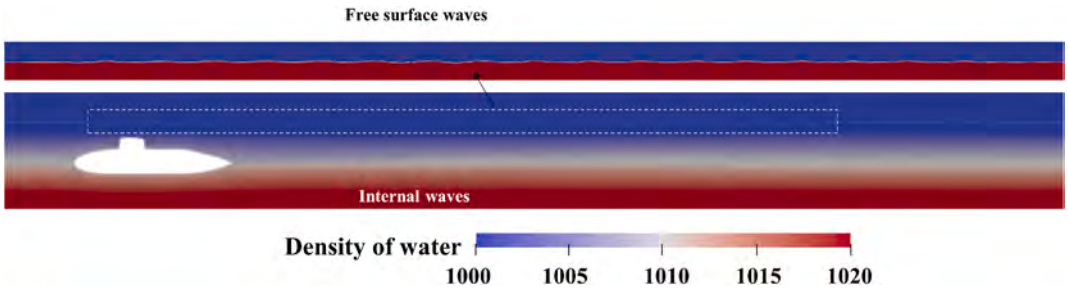

Fig. 20. Vertical free surface and internal wave profile in the stratified case.

Table 7
Measured Kelvin wedge angles in the stratified and homogeneous cases.

Description	Kelvin wedge angle (°)	Difference
Homogeneous case	≈19.5	–
Stratified case	≈22.5	+15.4%

and divergent waves consistent with the theoretical results mentioned in Yeung and Nguyen (1999). It can also be considered as the Kelvin wedge, which usually occurs in ship wave system.

In Fig. 17 and Table .6, when $t = 30$s, there are about 25 complete waveforms on the free surface in the stratified case, of which the maximum wave crest value is 0.0206 m, and the maximum wave trough value is 0.0174 m. Moreover, there are the same number of complete waveforms on the free surface in the homogeneous case, albeit with smaller values. The maximum wave crest value is 0.0117 m, and the maximum wave trough value is 0.0144 m. By comparing the value of the maximum wave crest, there is about a 20.8% increase in the stratified case. In contrast, refer to the maximum wave trough, the change surge to 76.1%. Additionally, the longitudinal and transverse propagation distances on the free surface are different in the homogenous and stratified cases.

In Table .6, the longitudinal propagation is about 63D, and the transverse propagation distance is about 38D in the homogeneous case. For the stratified case, the longitudinal propagation is about 68D, and the transverse propagation is about 43D. The waveform of the free surface in the stratified case has a longer and wider propagation distance in the x and y directions. The longitudinal propagation distance increases by 7.9%, and the transverse increases by 13.2%.

In short, stratification causes free surface waves to have a longer and wider influencing zone both in the x and y directions, including the longitudinal propagation distance increases by 7.9%, the transverse increases by 13.2%.

5.5.2. *Specific free surface profile analysis*

When analyzing the waveform on the free surface, it is essential to examine how the steady-state free surface profile varies with different cases. In each of these two cases, five x-z slices are created above the sail of the submarine at the free surface, which illustrated in Fig. 18. These slices are placed at $y/B = 0$, 0.25, 0.5, 0.75, and 1, where $y = 0$ corresponds to the mid-plane of the submarine, and $y = B$ corresponds to slices placed at a half breadth beyond the port and starboard edge of the submarine, B is the value of beam.

Fig. 19 shows the steady-state free surface profiles along the length of a submarine on each slice. In these images, the location of the submarine is [0, 6.7D], and we considered about 50D downstream evolution in the free surface.

One feature is clearly shown in Fig.19 (a) ~ (e) is that the free surface wave heights for the homogeneous and stratified simulations show typical oscillatory behavior. Due to stratification, the anisotropy of the wave height in the free surface is more obvious for the stratified case. The values of wave trough and wave crest in the homogeneous case are nearly in $z = 0$ symmetry, while in the stratified case, the values of the wave crest are slightly larger than the wave trough. Moreover, the wave trough and crest peak values in the stratified case are bigger than the homogeneous case. One possible explanation of the wave height difference between the homogeneous and stratified cases is the existence of internal waves. As the submarine displaces in a stably stratified fluid, the motion of itself disturbs the stable stratified background, and creates

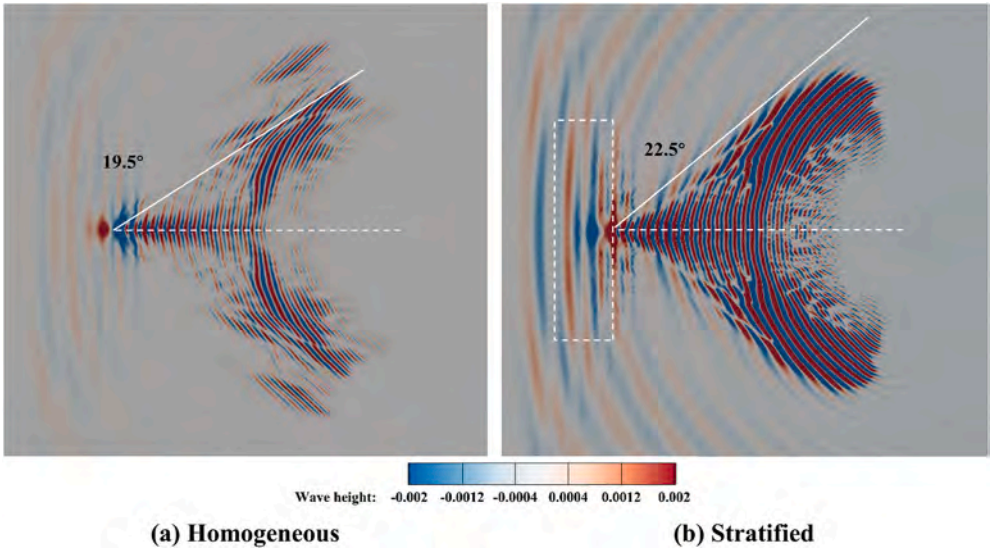

Fig. 21. The Kelvin wedge angle in the homogeneous and stratified cases.

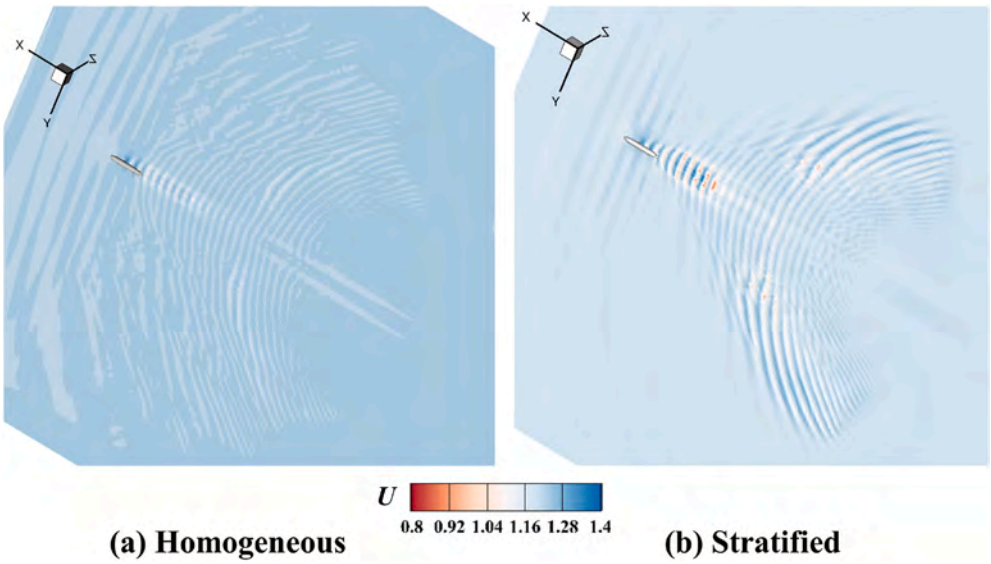

Fig. 22. View of axial velocity contour on the free surface of different cases.

internal waves and anisotropic turbulence that propagate downstream, as shown in Fig. 20. The generation of internal waves and downstream anisotropic turbulence provides a significant contribution to the anisotropy of the wave height in the free surface and the higher wave amplitude in the stratified case.

As mentioned before, this can also be seen in Fig.19 (a) ~ (e), in each picture, the propagation in the *x*-direction in stratified wakes is longer than in unstratified wakes. Besides this feature, the wave height defects in the *y*-direction in the stratified case are much smaller than in the homogeneous case, which means the characteristics on the free surface in the stratified case have a longer lifetime than in the unstratified case.

From this part, we can conclude that due to stratification, the wave height in the free surface clearly anisotropic and has a longer propagation distance in the *x* direction.

5.5.3. *Kelvin wedge angle and velocity on the free surface*

Table .7 shows the measured Kelvin wedge angles in each simulation and a measurement of the free surface wavelength along the symmetry plane of the submarine. We have measured the angle of the submarine's wakes from the images which extracted at the specific time ($t = 30$s). For each image, the wake angle is defined from the slope of the line going through the farthest points (white line), which traces the maximum amplitude of the wake. This method is the same as Rabaud and Moisy (2013) stated when estimating ship wakes of images, "the brightest points" now changed as the clearly visible points showed in the images. Thus, in Table .7, the kelvin wedge angle is an estimated value. It is found that the waveform of the stratified flow will gradually expand in the *x* and *y* directions, with the more significant value of Kelvin wedge angle. After about 20*D* downstream on the free surface, waves began expanding beyond the range of the Kelvin wedge angle, as shown in Fig. 21 (b). Moreover, in Fig. 21 (b), a blocking phenomenon can be seen in the stratified case, as shown in the dashed box. According to Lin et al. (1992), stratification induces upstream blocking, unlike in the unstratified case, the flow is vertically confined.

Additionally, we also analyze the contour of axial velocity on the free surface of different cases. In Fig. 22 (a) and (b), the trend of the axial velocity contour on the free surface looks the same as the Kelvin wedge angle. However, in Fig. 22 (b), the value of axial velocity in the stratified case appears higher. In a word, waves on the free surface in the stratified case have a longer and wider influencing zone relative to the unstratified counterpart.

Consistent with the previous conclusion, stratification would cause free surface waves to have a longer and wider influencing zone both in the *x* and *y* directions when referring to the Kelvin wedge angle and the velocity in the free surface, and the Kelvin wedge angle increase by 15.4%.

6. Conclusions

The present work mainly focuses on a weakly stratified fluid past a generic submarine model with $Re = 10^6$. We solved the Navier-Stokes equations under Boussinesq approximation, and proposed a thermocline model to achieve the linear density and temperature stratification. Four main aspects are chosen to discuss the specialty of stratified fluid characteristics by comparing the drag force, downstream wakes, internal waves, and free surface signatures with those of the homogeneous condition.

The results show that buoyancy in stratified fluid changes the vertical velocity and pressure gradient on the hull. Once the buoyancy effect works, stratification increases the resistance primarily by reducing the overall pressure in the rearward portion and increasing the pressure in the forward portion. The resistance in the stratified fluid increases about 5.5% when comparing the unstratified case.

Stratification also affects the establishment of the wakes and their downstream evolution. The vertical confinement by buoyancy in the stratified environment has caused the velocity to decay faster, and stratified wakes become wider than taller.

Besides the downstream wakes, internal waves and anisotropic turbulence produced by the moving submarine in the stratified environment can also influence the free surface characteristics. The heavier water will gradually float up downstream, which will contribute to the anisotropy of the wave height in the free surface and a longer and wider influencing zone on the free surface, including the longitudinal propagation distance increases by 7.9%, the transverse increases by 13.2%, and the Kelvin wedge angle increase by 15.4%.

CRediT authorship contribution statement

Fenglai Huang: Writing – original draft, Software, Data curation, Visualization. **Qingjie Meng:** Investigation, Formal analysis, Validation. **Liushuai Cao:** Conceptualization, Methodology, Writing – review & editing. **Decheng Wan:** Conceptualization, Supervision, Methodology, Project administration.

Declaration of competing interest

The authors declare that they have no known competing financial interests or personal relationships that could have appeared to influence the work reported in this paper.

Acknowledgements

This work is supported by National Natural Science Foundation of China (Nos. 52001210 and 52131102), the Oceanic Interdisciplinary Program of Shanghai Jiao Tong University (SL2020PT104), to which the authors are most grateful. Thanks to Prof. Pablo Carrica from The University of Iowa for providing the Joubert BB2 geometry and free running experimental data (Carrica et al., 2019, 2020).

References

Armenio, V., Sarkar, S., 2005. Environmental Stratified Flows, Courses and Lectures. Springer, Wien, ISBN 978-0-306-48024-9.
Barat, J., Cot, C., 1992. Wind shear rotary spectra in the atmosphere. Geophys. Res. Lett. 19, 103–106. https://doi.org/10.1029/92GL00044.
Bettle, M.C., 2020. Development of Computational Fluid Dynamics (CFD) Meshes for the BB2 Generic Submarine. Scientific Report, Defence Research and Development Canada.
Bonneton, P., Chomaz, J.M., Hopfinger, E.J., 1993. Internal waves produced by the turbulent wake of a sphere moving horizontally in a stratified fluid. J. Fluid Mech. 254, 23–40. https://doi.org/10.1017/S0022112093002010.
Boyer, D.L., Davies, P.A., Fernando, H.J.S., Zhang, X., Roberts, P.H., 1989. Linearly stratified flow past a horizontal circular cylinder. Philos. Trans. R. Soc. Lond. Ser. Math. Phys. Sci. 328, 501–528. https://doi.org/10.1098/rsta.1989.0049.
Brucker, K.A., Sarkar, S., 2010. A comparative study of self-propelled and towed wakes in a stratified fluid. J. Fluid Mech. 652, 373–404. https://doi.org/10.1017/S0022112010000236.
Cao, L., Zhu, J., Zeng, G., 2016. Viscous-flow calculations of submarine maneuvering hydrodynamic coefficients and flow field based on same grid topology. J. Appl. Fluid Mech. 9, 817–826. https://doi.org/10.18869/acadpub.jafm.68.225.24570.
Cao, L., Huang, F., Liu, C., Wan, D., 2021. Vortical structures and wakes of a sphere in homogeneous and density stratified fluid. J. Hydrodyn. 33, 207–215. https://doi.org/10.1007/s42241-021-0032-x.
Carrica, P.M., Kim, Y., Martin, J.E., 2019. Near-surface self propulsion of a generic submarine in calm water and waves. Ocean Eng. 183, 87–105. https://doi.org/10.1016/j.oceaneng.2019.04.082.
Carrica, P.M., Kerkvliet, M., Quadvlieg, F., Martin, J.E., 2020. CFD simulations and experiments of a submarine in turn, zigzag, and surfacing maneuvers. J. Ship Res. 1–16 https://doi.org/10.5957/JOSR.07200045.
Chase, N., Carrica, P.M., 2013. Submarine propeller computations and application to self-propulsion of DARPA Suboff. Ocean Eng. 60, 68–80. https://doi.org/10.1016/j.oceaneng.2012.12.029.
Chomaz, J.M., Bonneton, P., Hopfinger, E.J., 1993. The structure of the near wake of a sphere moving horizontally in a stratified fluid. J. Fluid Mech. 254, 1–21. https://doi.org/10.1017/S0022112093002009.
Chongsiripinyo, K., Pal, A., Sarkar, S., 2017. On the vortex dynamics of flow past a sphere at Re = 3700 in a uniformly stratified fluid. Phys. Fluids 29, 020704. https://doi.org/10.1063/1.4974503.
Chung, D., Matheou, G., 2012. Direct numerical simulation of stationary homogeneous stratified sheared turbulence. J. Fluid Mech. 696, 434–467. https://doi.org/10.1017/jfm.2012.59.
Diamessis, P.J., Spedding, G.R., Domaradzki, J.A., 2011. Similarity scaling and vorticity structure in high-Reynolds-number stably stratified turbulent wakes. J. Fluid Mech. 671, 52–95. https://doi.org/10.1017/S0022112010005549.
Dommermuth, D.G., Rottman, J.W., Innis, G.E., Novikov, E.A., 2002. Numerical simulation of the wake of a towed sphere in a weakly stratified fluid. J. Fluid Mech. 473, 83–101. https://doi.org/10.1017/S0022112002002276.
Donadei, C., 2019. Computational Fluid Dynamics Predictions of Submarine Hydrodynamics. MSc thesis, ENSTA Bretagne.
Esmaeilpour, M., 2017. A ship advancing in a stratified fluid: the dead water effect. In: Doctoral Thesis, the University of Iowa.
Gao, T., Wang, Y., Pang, Y., Chen, Q., Tang, Y., 2018. A time-efficient CFD approach for hydrodynamic coefficient determination and model simplification of submarine. Ocean Eng. 154, 16–26. https://doi.org/10.1016/j.oceaneng.2018.02.003.
Gourlay, M.J., Arendt, S.C., Fritts, D.C., Werne, J., 2001. Numerical modeling of initially turbulent wakes with net momentum. Phys. Fluids 13, 3783–3802. https://doi.org/10.1063/1.1412246.
Hirt, C.W., Nichols, B.D., 1981. Volume of fluid (VOF) method for the dynamics of free boundaries. J. Comput. Phys. 39, 201–225. https://doi.org/10.1016/0021-9991(81)90145-5.
Hopfinger, E.J., Flor, J.-B., Chomaz, J.-M., Bonneton, P., 1991. Internal waves generated by a moving sphere and its wake in a stratified fluid. Exp. Fluid 11, 255–261. https://doi.org/10.1007/BF00192753.
Joubert, P.P.N., 2006. Some Aspects of Submarine Design - Part 2. Shape of a Submarine 2026.
Kumar, P., Mahesh, K., 2018. Large-eddy simulation of flow over an axisymmetric body of revolution. J. Fluid Mech. 853, 537–563. https://doi.org/10.1017/jfm.2018.585.
Li, J., Martin, J.E., Carrica, P.M., 2019. Large-scale simulation of ship bubbly wake during a maneuver in stratified flow. Ocean Eng. 173, 643–658. https://doi.org/10.1016/j.oceaneng.2019.01.001.
Lin, J.T., Pao, Y.H., 1979. Wakes in stratified fluids. Annu. Rev. Fluid Mech. 11, 317–338. https://doi.org/10.1146/annurev.fl.11.010179.001533.
Lin, Q., Lindberg, W.R., Boyer, D.L., Fernando, H.J.S., 1992. Stratified flow past a sphere. J. Fluid Mech. 240, 315. https://doi.org/10.1017/S0022112092000119.
Liu, S., He, G., Wang, Z., Luan, Z., Zhang, Z., Wang, W., Gao, Y., 2020. Resistance and flow field of a submarine in a density stratified fluid. Ocean Eng. 217, 107934. https://doi.org/10.1016/j.oceaneng.2020.107934.
Ma, W., Li, Y., Ding, Y., Hu, K., Lan, L., 2018. Numerical simulations of linearly stratified flow past submerged bodies. Pol. Marit. Res. S 3. https://doi.org/10.2478/pomr-2018-0114.
Ma, W., Li, Y., Ding, Y., Duan, F., Hu, K., 2020. Numerical investigation of internal wave and free surface wave induced by the DARPA Suboff moving in a strongly stratified fluid. Ships Offshore Struct. 15, 587–604. https://doi.org/10.1080/17445302.2019.1661633.
Menter, F.R., Kuntz, M., 2004. Adaptation of eddy-viscosity turbulence models to unsteady separated flow behind vehicles. In: McCallen, R., Browand, F., Ross, J. (Eds.), The Aerodynamics of Heavy Vehicles: Trucks, Buses, and Trains, Lecture Notes in Applied and Computational Mechanics. Springer, Berlin, Heidelberg, pp. 339–352. https://doi.org/10.1007/978-3-540-44419-0_30.
Mercier, M.J., Wang, S., Péméja, J., Ern, P., Ardekani, A.M., 2020. Settling disks in a linearly stratified fluid. J. Fluid Mech. 885 https://doi.org/10.1017/jfm.2019.957.
Meunier, P., Diamessis, P.J., Spedding, G.R., 2006. Self-preservation in stratified momentum wakes. Phys. Fluids 18, 106601. https://doi.org/10.1063/1.2361294.
Niu, M., Ding, Y., Ma, W., Han, P., 2017. Research on the numerical simulation methods of continuously stratified flows based on thermal density current model. J. Ship Mech. 21 (08), 941–949. https://doi.org/10.3969/j.issn.1007-7294.2017.08.002 (In Chinese).
Orr, T.S., Domaradzki, J.A., Spedding, G.R., Constantinescu, G.S., 2015. Numerical simulations of the near wake of a sphere moving in a steady, horizontal motion through a linearly stratified fluid at Re = 1000. Phys. Fluids 27, 035113. https://doi.org/10.1063/1.4915139.
Ortiz-Tarin, J.L., Chongsiripinyo, K.C., Sarkar, S., 2019. Stratified flow past a prolate spheroid. Phys. Rev. Fluids 4, 094803. https://doi.org/10.1103/PhysRevFluids.4.094803.
Pal, A., Sarkar, S., Posa, A., Balaras, E., 2016. Regeneration of turbulent fluctuations in low-Froude-number flow over a sphere at a Reynolds number of 3700. J. Fluid Mech. 804 https://doi.org/10.1017/jfm.2016.526.
Pal, A., Sarkar, S., Posa, A., Balaras, E., 2017. Direct numerical simulation of stratified flow past a sphere at a subcritical Reynolds number of 3700 and moderate Froude number. J. Fluid Mech. 826, 5–31. https://doi.org/10.1017/jfm.2017.398.
Pedlosky, J., 1979. Geophysical Fluid Dynamics. Springer US, New York, NY. https://doi.org/10.1007/978-1-4684-0071-7.
Posa, A., Balaras, E., 2020. A numerical investigation about the effects of Reynolds number on the flow around an appended axisymmetric body of revolution. J. Fluid Mech. 884, A41. https://doi.org/10.1017/jfm.2019.961.
Rabaud, M., Moisy, F., 2013. Ship wakes: kelvin or Mach angle? Phys. Rev. Lett. 110, 214503. https://doi.org/10.1103/PhysRevLett.110.214503.
Sakamoto, H., Haniu, H., 1990. A study on vortex shedding from spheres in a uniform flow. J. Fluid Eng. 112, 386–392. https://doi.org/10.1115/1.2909415.
Spedding, G.R., 1997. The evolution of initially turbulent bluff-body wakes at high internal Froude number. J. Fluid Mech. 337, 283–301. https://doi.org/10.1017/S0022112096004557.
Spedding, G.R., 2014. Wake signature detection. Annu. Rev. Fluid Mech. 46, 273–302. https://doi.org/10.1146/annurev-fluid-011212-140747.
Srdić-Mitrović, A.N., Mohamed, N.A., Fernando, H.J.S., 1999. Gravitational settling of particles through density interfaces. J. Fluid Mech. 381, 175–198. https://doi.org/10.1017/S0022112098003590.
Sysoeva, E., Chashechkin, Y., 1991. Vortex systems in the stratified wake of a sphere. Fluid Dynam. 26, 544–551. https://doi.org/10.1007/BF01050316.
Taitel, Y., Barnea, D., Brill, J.P., 1995. Stratified three phase flow in pipes. Int. J. Multiphas. Flow 21, 53–60. https://doi.org/10.1016/0301-9322(94)00058-R.
Torres, C.R., Hanazaki, H., Ochoa, J., Castillo, J., Van Woert, M., 2000. Flow past a sphere moving vertically in a stratified diffusive fluid. J. Fluid Mech. 417, 211–236. https://doi.org/10.1017/S0022112000001002.
Torunski, B., 2016. Computational Analysis of the Free Surface Effects on a BB2 Submarine Undergoing Horizontal Maneuvers. MSc thesis, The University of New Brunswick.
Wei, G., Lu, D., Dai, S., 2005. Waves induced by a submerged moving dipole in a two-layer fluid of finite depth. Acta Mech. Sin. 21, 24–31. https://doi.org/10.1007/s10409-004-0003-9.
Wei, G., Lu, D., Su, X., You, Y., 2009. Experimental study on time series structures of the wake in a linearly stratified fluid. Sci. Sin. (Phys. Mech. Astronom.) 39 (09) (In chinese).
Xue, F., Jin, W., Qiu, S., Yang, J., 2020. Wake features of moving submerged bodies and motion state inversion of submarines. IEEE Access 8, 12713–12724. https://doi.org/10.1109/ACCESS.2020.2966005.
Yeung, R.W., Nguyen, T.C., 1999. Waves generated by a moving source in a two-layer ocean of finite depth. J. Eng. Math. 35, 85–107. https://doi.org/10.1023/A:1004399917692.

Yun, G., Kim, D., Choi, H., 2006. Vortical structures behind a sphere at subcritical Reynolds numbers. Phys. Fluids 18, 015102. https://doi.org/10.1063/1.2166454.
Zhang, D., Chao, L., Pan, G., 2019. Analysis of hydrodynamic interaction impacts on a two-AUV system. Ships Offshore Struct. 14, 23–34. https://doi.org/10.1080/17445302.2018.1472518.
Zhihua, L., Ying, X., Chengxu, T., 2011. Numerical simulation and control of horseshoe vortex around an appendage–body junction. J. Fluid Struct. 27, 23–42. https://doi.org/10.1016/j.jfluidstructs.2010.08.006.